



HAL
open science

Parametric study on state-of-the-art analytical models for fan broadband interaction noise predictions

Danny Lewis, Jérôme de Laborderie, Marlène Sanjosé, Stéphane Moreau,
Marc Jacob, Vianney Masson

► **To cite this version:**

Danny Lewis, Jérôme de Laborderie, Marlène Sanjosé, Stéphane Moreau, Marc Jacob, et al.. Parametric study on state-of-the-art analytical models for fan broadband interaction noise predictions. Journal of Sound and Vibration, 2021, 10.1016/j.jsv.2021.116423 . hal-03334251

HAL Id: hal-03334251

<https://hal.science/hal-03334251>

Submitted on 16 Oct 2023

HAL is a multi-disciplinary open access archive for the deposit and dissemination of scientific research documents, whether they are published or not. The documents may come from teaching and research institutions in France or abroad, or from public or private research centers.

L'archive ouverte pluridisciplinaire **HAL**, est destinée au dépôt et à la diffusion de documents scientifiques de niveau recherche, publiés ou non, émanant des établissements d'enseignement et de recherche français ou étrangers, des laboratoires publics ou privés.



Distributed under a Creative Commons Attribution - NonCommercial 4.0 International License

Parametric Study On State-of-the-Art Analytical Models for Fan Broadband Interaction Noise Predictions

Danny Lewis^{a,*}, Jérôme de Laborderie^b, Marlène Sanjosé^c, Stéphane Moreau^d, Marc C. Jacob^a,
Vianney Masson^d

^a*Univ Lyon, Ecole Centrale de Lyon, INSA Lyon, Université Claude Bernard Lyon I, CNRS, Laboratoire de Mécanique des Fluides et d'Acoustique, UMR 5509, 36 Avenue Guy de Collongue, F-69134, Ecully, France*

^b*Safran Aircraft Engines, 77550 Moissy-Cramayel, France*

^c*Département de Génie Mécanique, École de Technologie Supérieure, Montréal, QC, H3C 1K3, Canada*

^d*Département de Génie Mécanique, Université de Sherbrooke, Sherbrooke, QC, J1K2R1, Canada*

Abstract

Rotor-Stator Interaction (RSI) noise predictions using analytical models have become a first hand approach to perform quick and efficient noise assessments. However, a large range of models using different assumptions is currently available and it is of paramount interest to investigate what their impact on the predictions are and how representative of the real configuration they are. The present work proposes to study the impact of such assumptions on predictions using analytical models informed with RANS flow simulations. It focuses on four models which represent the state of the art of RSI noise prediction for fan-Outlet Guide Vane (OGV) stages: Ventres' model, Hanson's model, Posson's model and Masson's model. These models are tested on the NASA Source Diagnostic Test (SDT) baseline case at approach condition. A sensitivity study is carried out to identify and explain the discrepancies introduced by the assumptions made in the models. It is shown that the geometry definition (staggered flat plate), the definition of the impinging flow (2D or 3D, modeling of turbulence), the computation of the acoustic sources (2D or 3D response, isolated or cascade response), as well as the sound radiation method (free-field or in-duct propagation with mean axial or swirling flow) have a substantial impact on the predictions. The impact of the differences in the input quantities extracted from two different RANS simulations is also assessed, showing an important effect of background and wake turbulence intensities as well as of the turbulence integral length scale. The present work also demonstrates that the use of anisotropic turbulence models, which may become more common in the future due to the evolution of engine architectures, must be done carefully because of the sensitivity of the models to the anisotropic parameters which are difficult to assess from RANS simulations.

Keywords: aeroacoustics, turbomachinery, rotor-stator interaction, broadband noise, fan noise, analytical modeling.

1. Introduction

The constant growth in air transport coupled with the strengthening of noise regulations have turned noise pollution into a major concern for aircraft manufacturers. Significant aircraft

*Corresponding author

Email addresses: danny.lewis@onera.fr (Danny Lewis), jerome.de-laborderie@safrangroup.com (Jérôme de Laborderie), Marlene.Sanjose@etsmtl.ca (Marlène Sanjosé), stephane.moreau@usherbrooke.ca (Stéphane Moreau), marc.jacob@ec-lyon.fr (Marc C. Jacob), vianney.masson@gmail.com (Vianney Masson)

Nomenclature

Latin characters

c	Blade/vane chord
d	Non-overlapping area
h	Intervane channel height
R_{Hub}	Radius at the stator hub
R_{Tip}	Radius at the stator tip
w	Upwash velocity fluctuation

Greek characters

χ	Stagger angle
Σ	Solidity of the blade row
σ	Interblade phase angle

Acronyms

$2D$	Two dimensional
$3D$	Three dimensional
CFD	Computational Fluid Dynamics
LE	Leading-Edge
OGV	Outlet Guide Vane
$RANS$	Reynolds averaged Navier-Stokes
RSI	Rotor-Stator Interaction
SDT	Source Diagnostic Test
SWL	Sound Power Level
TE	Trailing-Edge
TI	Turbulence Intensity
TLS	Turbulence Length Scale

noise reductions have already been achieved mostly by increasing the bypass ratio of the engines, leading to a substantial decrease in the jet noise. The development of passive noise control technologies, such as acoustic liners, also led to significant noise reductions, mostly regarding its tonal component. However, in order to sustain the foreseen increase in air transport, further improvements need to be made. One candidate to further decrease noise pollution, while maintaining the fuel burn reduction trend, is the Ultra-High Bypass Ratio engine (UHBR). This solution is basically an extension of current turbofan engine architectures: it displays a larger diameter, resulting in an increased bypass ratio, and a shorter nacelle to compensate the weight and drag penalties that would arise from the engine widening. In such architectures, the fan stage is expected to become a major contributor to the total radiated noise at all certification points, with a dominant broadband noise component. This noise component originates from random fluctuating mechanisms in the engine. More precisely, in Fan-Outlet Guide Vane (OGV) stages, it results from the interaction of turbulent structures with solid walls involved in inlet turbulence ingestion, turbulent boundary layers, tip gap vortex and in the impingement of the fan wakes onto the OGVs. The latter mechanism is referred to as the rotor-stator interaction (RSI) mechanism and has been identified as the dominant mechanism responsible for broadband noise generation within a fan stage. Therefore, reducing the impact of this mechanism appears to be a direct way to tackle the problem of aircraft noise pollution. Developing new methods and tools that would enable accurate predictions then becomes a necessity.

Analytical models appear to be an efficient tool to predict broadband RSI noise. The inherent mathematical simplifications made in these models associated with the very low computational cost make analytical models a first hand tool to quickly provide noise estimates [1, 2] and carry out optimization studies [2]. These characteristics are particularly useful in the early stage of development of new engines [3], when the exact geometry is yet to be defined and no detailed simulation can be performed. Additionally, analytical models can be coupled with low order simulations (such as RANS simulations [4, 1]) to provide more accurate results in a reasonable time with respect to high order simulations such as Large Eddy Simulations (LES).

Since broadband noise results from the impingement and the scattering of turbulent structures on blades, vanes and walls, its prediction can be more challenging than for the tonal noise as it involves a large range of scales particularly at the high Reynolds number at which UHBR engines operate.

There are numerous analytical models which aim at predicting the fan broadband interaction

noise [5, 6]. Each model endeavors to describe the noise resulting from the interaction of turbulent structures (wake and background turbulence) with a vane cascade. Some of them are empirical [7, 8], but the present article exclusively focuses on physics based models which basically aim at modeling the noise sources resulting from the RSI mechanism, and use them in the framework of some form of acoustic analogies.

The early models were focusing on the interaction of a perturbation impinging onto an isolated airfoil. In this type of model, an incident gust normal to the vane is convected until it reaches its Leading-Edge (LE), creating an unsteady loading [that is compensated by a resulting broadband sound field in order to fulfill the impermeability condition of the solid plates](#). Sears [9] first formulated an isolated airfoil model in the specific case of incompressible flows, only valid at low frequency. Amiet developed a compressible response function [10], [first](#) extended by Paterson and Amiet [11], to take into account Trailing-Edge (TE) back-scattering, and then by Moreau *et al.* [12] and Roger *et al.* [13] to [account for](#) three-dimensional (3D) aerodynamic gusts with subcritical and supercritical gusts. In these models, the airfoil is modeled as an infinitely thin flat plate immersed in a uniform inviscid flow with zero incidence, neglecting camber and mean loading effects. [The latter effect were then introduced by Myers and Kerschen \[14, 15\] and Evers and Peake \[16\] using asymptotic theories and the Rapid Distortion Theory](#). These models are [appropriate for predicting](#) the broadband noise radiated by low solidity rotors without external casing such as helicopter rotors or propellers. However, modern ducted fan-OGV stages now display a significant number of vanes with substantial overlapping, questioning the isolated vane assumption. In such a configuration, the influence of the neighboring vanes on the acoustic propagation, which one can refer to as cascade effect, cannot be neglected anymore.

A new range of models have therefore been developed to take the cascade effect into account. They all aim at resolving the integral equation of the problem using different approaches and different levels of modeling. The first models solved this equation numerically considering only a two-dimensional (2D) rectilinear cascade configurations, using the lifting surface method (equally called "singularity method") that can be based, for instance, on the discontinuity of the acceleration potential (Kaji and Okazaki [17]), on the pressure jump across a vane (Whitehead [18, 19]) or even on the chordwise axial velocity discontinuity through a vane cascade (Smith [20]). The latter model eventually led to the creation of the code LINSUB (LINearised SUBsonic unsteady flow in cascade), which has been extensively used by Cheong *et al.* [21], Jurdic *et al.* [22] and Lloyd and Peake [23] for instance. All previously mentioned approaches share important characteristics:

- The considered incident flow is two-dimensional.
- The cascade response is consequently two-dimensional and is obtained by numerically solving an integral equation. This implies, in most cases, to resort to a collocation method, which negatively impacts the computational cost of the model.
- The sound propagation does not account for the effect of the duct walls.

Considering this, Goldstein [24] developed a method to model three-dimensional gusts and to compute the subsequent three-dimensional cascade response. Goldstein [25] also developed the formalism to account for duct wall effects on the acoustic propagation. These improvements were later used by Atassi and Hamad [26] to model the RSI mechanism. Their study notably revealed the importance of three-dimensional effects on the radiated acoustic power. In parallel of these rectilinear cascade models, Namba [27, 28], Kodama and Namba [29] and Schulten [30, 31] developed their own models based on a singularity method for a ducted three-dimensional annular cascade. However, these models assume a null stagger angle, which leads to a bias in the intake/exhaust acoustic propagation.

Another category of models numerically solves the integral equation of the problem to obtain the cascade response, that is then used as an equivalent dipole source in the framework of an acoustic analogy to propagate the produced noise. This is the case of Ventres' model [32], which uses a collocation method to compute this integral considering a 2D flow impinging onto an annular cascade. In this model, the real distribution of the acoustic sources over the vanes is computed and used within an acoustic analogy considering an infinite annular duct with a constant axial mean flow. Such an analogy is based on Goldstein's Green's function for circular duct (see Eq. (1.77) in [24]) extended to the case of an annular duct, and is often referred to as Goldstein's analogy. More details on this analogy are provided by Pérez Arroyo *et al.* [33] and Posson *et al.* [34]. This model has been successively enhanced by Meyer and Envia [35], Nallasamy and Envia [36], and Grace *et al.* [37, 38, 39, 40], resulting in a model called RSI that eventually takes into account three-dimensional gusts.

Another branch of models, which analytically solves this equation through the use of the Wiener-Hopf technique, also emerged. This method was initially introduced and extended by Mani and Hovray [41], Koch [42], Peake [43, 44] and Glegg [45]. Glegg notably developed a three-dimensional cascade response that does not rely on the direct computation of the acoustic sources on the vanes to obtain the acoustic field outside of the cascade. Glegg's model was then extended by Hanson and Horan [3] and by Hanson [46], who developed a model that uses a new formalism to take complex geometry features into account and, as in Ventres' model, takes the spanwise variations of the flow and the blade into account through the use of the strip theory. Posson *et al.* [47, 48] extended Glegg's cascade response to the computation of the unsteady loading on the vanes. They included Hanson's enhancements regarding the handling of complex geometries and the use of the strip theory. As in Ventres' model, the computed unsteady loading is used as a dipole source in Goldstein's analogy. Posson's model can then be seen as an analytical version of Ventres' model extended to three-dimensional gusts. Masson *et al.* [49] eventually extended Posson's model by accounting for swirl using the generalized Green's function proposed by Posson and Peake [50] for homentropic flows. Mathews and Peake also recently developed a Green's function accounting for swirl but for a more general isentropic flow with a lined duct [51]. Other studies have also addressed the case of more realistic airfoil geometries. For instance, Baddoo *et al.* [52, 53] developed a model that takes into account both the camber and the thickness of the airfoil, the values of which being bounded by asymptotic restrictions. They assumed that the upper and lower surfaces of the blade, $\epsilon y_{s\pm}$, could be described by $\epsilon y_{s\pm}(x) = \pm \epsilon y_{th}(x) + \epsilon y_c(x)$, where the subscripts c and th denote camber and thickness respectively and $\epsilon \ll 1$. This restricts the model to thin airfoils so that background flow gradients are $O(\epsilon)$ perturbations from uniformity. The frequency must also satisfy $k\epsilon \ll 1$, where k is the reduced frequency, which is not that restrictive in the case of fan-OGV stages. By testing a variety of airfoil geometries, they have demonstrated that these parameters have a significant impact on the actual radiated noise both upstream and downstream of the cascade.

In parallel, some models resorting to the mode-matching approach have been developed. This technique is based on modal expansions in various subdomains of the stator row [5]. Bouley *et al.* [54] proposed such a model and applied it to the impingement of rotor wakes onto a 2D rectilinear cascade, showing results identical to those obtained with the Wiener-Hopf technique from Posson *et al.* [47, 48]. François *et al.* [55] extended this model to the prediction of the noise resulting from the turbulence impingement onto a zero-stagger three-dimensional annular vane cascade in a uniform flow, with no spanwise variations of the turbulent quantities. This was achieved without the use of the strip theory, allowing to completely take the radial mode scattering into account as well as the non-parallelism of the vanes, which are neglected in the strip theory. Additional work is currently being carried out by Girier *et al.* [56] to consider the curvature of the vane in order to model the vane geometry more precisely.

Figures 1 and 2 show two diagrams explaining the history of the papers cited above for

the isolated airfoil response and the cascade response, respectively. These diagrams are not exhaustive but give a better view of how the different studies are related.

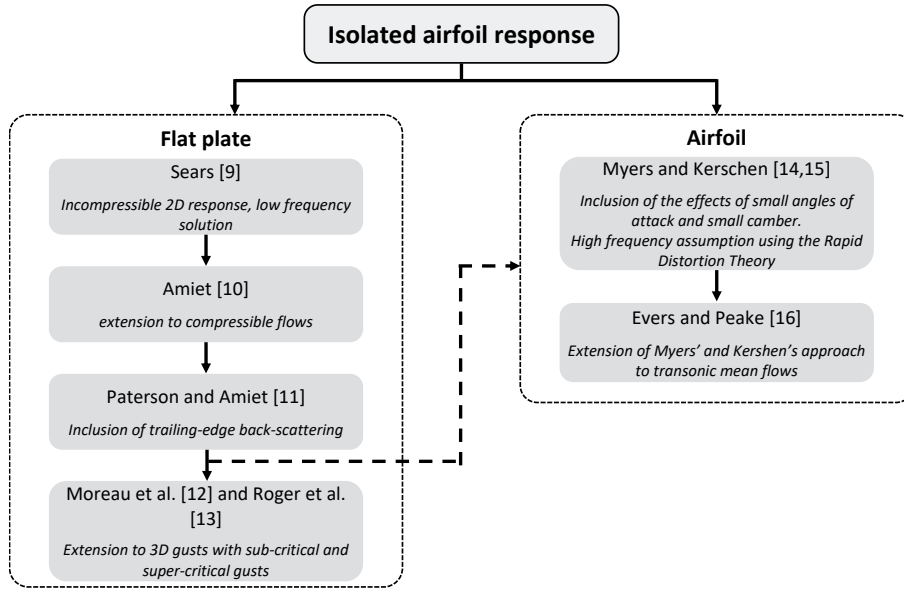


Figure 1: Classification of isolated airfoil models.

The present article focuses on coupling RANS simulations with five models: four models taking into account the cascade effect (Ventres’ model, Hanson’s model, Posson’s model and Masson’s model) and one model using an isolated blade response (Amiet’s model). It aims at identifying and explaining part of the discrepancies observed when performing RANS-based analytical predictions using these five models. The objective is to investigate the impact on the noise predictions of some assumptions made in these models regarding the geometry definition (staggered flat plate), the definition of the impinging flow (2D or 3D, modeling of turbulence), the computation of the acoustic sources (2D or 3D response, isolated vane or cascade response), and the sound radiation method (free-field or in-duct propagation, with axial mean flow or swirling flow). In the next section, a brief review of the specific features of each model is given. The NASA Source Diagnostic Test (SDT) as well as the RANS simulations that were performed on this test case are then presented in Section 3. Finally, Section 4 gathers all the parametric studies performed for each model building block.

2. Analytical models for broadband noise prediction

In this section, four cascade analytical models representing the state of the art of fan-OGV broadband interaction noise prediction are presented: the model of Posson *et al.* [47, 48], the model of Hanson [3, 57], the model of Masson [49], and the model of Ventres [32]. Amiet’s model [10, 11] is also presented as it is used as a comparison tool in the following sections. The aim of this section is to give a comprehensive overview of these models without going in depth in the mathematical formulation. The specific features of each model are then depicted in order to identify the sources of possible discrepancies between the results obtained from them.

2.1. Overview of analytical models

As highlighted by Ffowcs Williams and Hawkings [58], and Goldstein [59], the dominant noise source in a subsonic ducted fan-OGV is the unsteady loading on the vanes, which corresponds to a surface distribution of dipole sources. Indeed, for such operating points, the acoustic power

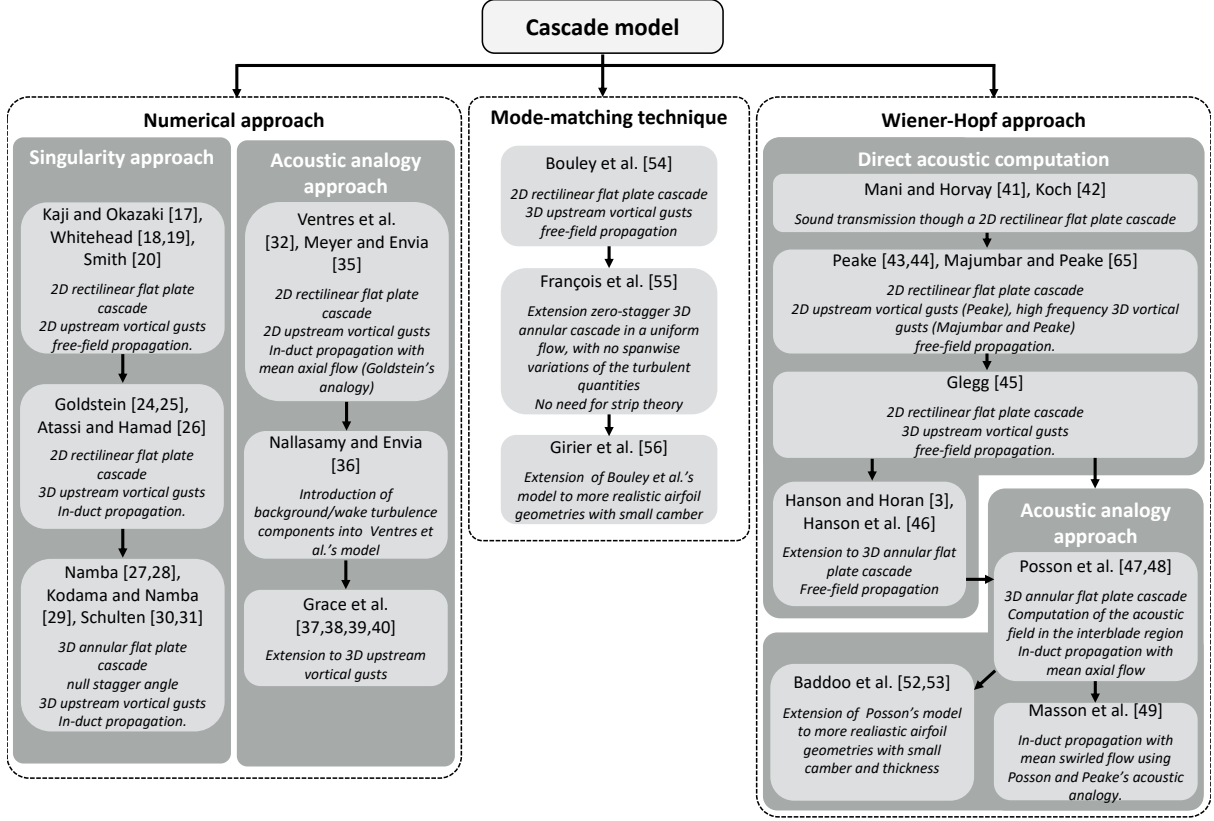


Figure 2: Classification of cascade models.

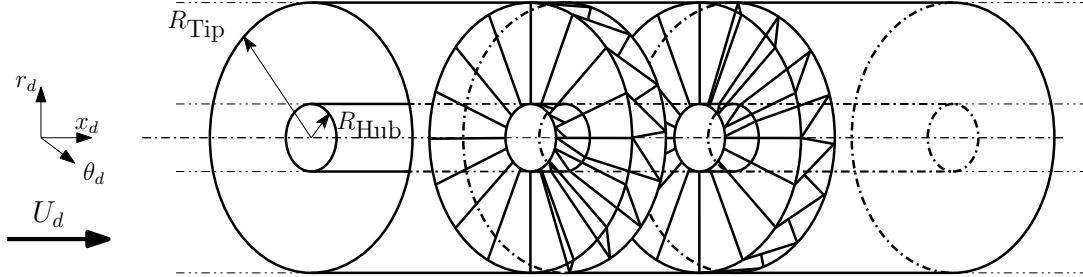


Figure 3: Fan stage configuration for the acoustic models.

emitted by a volume of quadrupole sources P_Q scales as $P_Q \sim M^2 P_D$, where M is the average Mach number of the considered flow, and P_D the power emitted by surface dipoles (see Section 3.3.4.2.2 in [59]). Hence, for low Mach numbers, quadrupole sources appear as negligible with respect to dipole sources. Consequently, the main aim of analytical models is to compute the unsteady loading on the vanes, resulting from the turbulent rotor wake impingement, in order to compute the far-field acoustic power at intake and exhaust using an acoustic analogy. A similar global approach consisting of four main steps is followed by these models as described by Moreau & Roger [5] and by Moreau [6, 2], and summarized below:

- The geometry definition: all the models consider a fan stage in an infinite annular duct (Figure 3) in which rotor blades and stator vanes are modeled as zero thickness flat plates with finite chord and span. The equivalent flat plate radial evolution matches the pitch and spanwise stackings of the real geometry and preserves some of the main geometrical parameters involved in the blade design, such as the stagger, lean and sweep angles,

that have a significant effect on both the tonal and the broadband noise [60, 61]. Other parameters inherent to the cascade such as the chord length c , the intervane channel height h , the parameter $s = 2\pi r_m/V$ (with r_m the mean radius and V the number of vanes), the solidity $\Sigma = c/s$ and the non-overlapping area d as shown in Fig. 5 are also replicated with this approach. The geometry is then split into cylindrical strips (strip theory) at radius r which have a finite radial extent Δr over which the geometric parameters are considered homogeneous. Every strip is then unwrapped into a rectilinear cascade with an infinite number of vanes to ensure periodicity.

- The definition of the [impinging flow/upstream disturbance](#): in this step, the input parameters of the models are defined. These parameters aim at replicating as closely as possible the main flow features that govern the broadband noise generation and propagation such as the mean flow in the duct, the mean velocity deficit within the wake or the incident turbulence. To do so, the radial evolution of the axial velocity, the absolute velocity, the wake half-width as well as the wake and background turbulence are used as inputs of the models. The turbulence is described by two parameters, the integral length scale and the turbulence intensity, either separately in the wake and in the background flow, or averaged across all azimuthal directions. Additionally, since [random/chaotic](#) phenomena are the cause of broadband noise, a statistical treatment through the use of a [power spectral density](#) is required to describe the turbulent behavior of the flow. The latter point is further detailed in Section 4.2.3. Within each strip determined in the geometry definition, the previously identified flow parameters are [assumed](#) constant. At each strip, the real incident flow is modeled as a gust convected by a mean flow in the form of a harmonic perturbation by time and spatial Fourier transforms, defined by the mean and turbulent characteristics of the flow at the considered radius. Depending on the model, the incident flow can be modeled using 2D gusts, taking the two components of the wave number in the cascade plane into account, or using 3D gusts by considering a third wave number component in the spanwise direction. This choice has a [significant](#) impact on the predicted noise as will be seen in section 4.2.2.
- The computation of the acoustic sources: the vane or cascade response is then computed, providing the unsteady loading distribution on the vane [resulting from the impingement of the upstream disturbance onto the vanes](#). As detailed in [5], for configurations displaying large values of h/c and of overlap ($c-d$), and small solidity Σ , such as propellers or Counter Rotating Open Rotors (CROR), the unsteady loading can be computed using an isolated airfoil model. However, for ducted propulsion systems on which the present study focuses, the solidity and the overlap are more substantial, especially for the Outlet Guide Vane (OGV), which requires the use of cascade responses that take the neighboring vanes into account to compute the unsteady loading.
- The sound radiation : the computed unsteady lift is then used as an equivalent dipole source in a chosen acoustic analogy to recover the acoustic power upstream and downstream of the studied cascade. Different types of acoustic analogies can be used to best suit the studied configuration taking its specific features into account, among which the presence of duct walls or of a [swirling](#) flow in the interstage can be mentioned. These constraints [lead](#) to multiple acoustic analogies such as a free-field analogy with a uniform mean flow (as in Hanson’s model in section 2.4.1), an in-duct analogy with a uniform mean axial flow (see Ventres’ and Posson’s models in section 2.3 and 2.4.2 respectively) or even an in-duct analogy with a mean [swirled](#) flow as recently proposed by Masson *et al.* [49] (see section 2.4.3).

As mentioned above, the strip theory approach must be used along with these models to

predict the noise of a 3D annular configuration. This approach is only valid for flows with a small radial velocity component, which is a fair assumption as stated by Meyer and Envia [35] who showed that, for an axial turbo-machine, the radial component of the flow becomes negligible only a half-chord downstream of the rotor. Additionally, the lack of parallelism between adjacent blades as well as the radial scattering cannot be accounted for with this type of approach.

Furthermore, the amplitude of the impinging perturbations as well as the one of the cascade response are considered small with respect to the mean flow which enables to restrict the analysis to a linearized problem. The viscosity of the fluid is also neglected. Indeed, as detailed in [5], the radiated noise originates from the interactions between vortical perturbations and solid surfaces. These interactions are significantly faster than the characteristic lifetime of the perturbations, which leads to a negligible effect of the viscosity with respect to the inertial effects. As a consequence, viscosity is not considered in the interaction mechanisms, except at the TE where the modeling of the wake is ensured through the use of a Kutta condition. These assumptions allow to consider the convected Helmholtz equation as the main foundation of the models that are presented in the following sections.

The models discussed hereafter follow this global approach, in the scope of linear theory, with their own specific features. They particularly differ in the modeling of the incident flow, the method to compute the unsteady lift on each strip, and the type of acoustic analogy.

2.2. Amiet's model

Amiet's model provides the response of an isolated zero-thickness flat plate immersed in an inviscid uniform flow $(U_{xc}, 0, 0)$ to the impingement of an upstream upwash velocity fluctuation normal to its chord. The flat plate chord and span are $2b$ and $2d$, respectively, and the origin of the coordinate system is located at the center of the flat plate (see Figs. 4a and 4b). Let w be an upstream disturbance in the form of a three-dimensional harmonic gust of pulsation ω , which can be written as follows:

$$w(x_c, z_c) = w_0 e^{-i\omega t} e^{i(k_{xc}x_c + k_{zc}z_c)}, \quad (1)$$

where k_{xc} and k_{zc} are the wave numbers along the directions x_c and z_c respectively. w does not depend on k_{yc} , the wave number component normal to the flat plate chord, since the flat plate is located in the plane $y = 0$. Under these assumptions, the distribution of the pressure jump can be written as [10]:

$$\Delta p_0(x, z, t) = 2\pi\rho_\infty b U_{xc} w_0 g(x, k_{xc}, k_{zc}) e^{-i\omega t} e^{ik_{zc}z}, \quad (2)$$

where $g(x, k_{xc}, k_{zc})$ is the transfer function between the impacting gust and the airfoil pressure jump. This function can be computed through a two step iterative process. First, the pressure distribution on the flat plate due to the leading edge scattering is computed assuming a semi-infinite flat plate. This pressure distribution is then corrected by a trailing-edge back-scattering contribution which fully accounts for the finite chord length. This process is run until convergence is reached, providing the relationship of g . In the original model of Amiet, the pressure jump is then used to compute the resulting far-field power spectral density which reads:

$$S_{PP}(x, y, z, \omega) = \left(\frac{\omega y \rho_0 b}{c_0 \sigma^2} \right)^2 U d \pi \int_{-\infty}^{\infty} \left[\frac{\sin^2(d(k_{zc} + \omega z / c_0 \sigma))}{(k_{zc} + \omega z / c_0 \sigma)^2 \pi d} \right] |\mathcal{L}(x, k_{xc} = \omega / U_{xc}, k_{zc})|^2 \times \Phi_{ww}(k_{xc} = \omega / U_{xc}, k_{yc}, k_{zc}) dk_{zc}, \quad (3)$$

where $\mathcal{L}(x, k_{xc}, k_{zc})$ is the total aeroacoustic transfer function computed using the normalized pressure jump $g(x, k_{xc}, k_{zc})$, and $\Phi_{ww}(k_{xc}, k_{yc}, k_{zc})$ the turbulence spectrum of the upwash

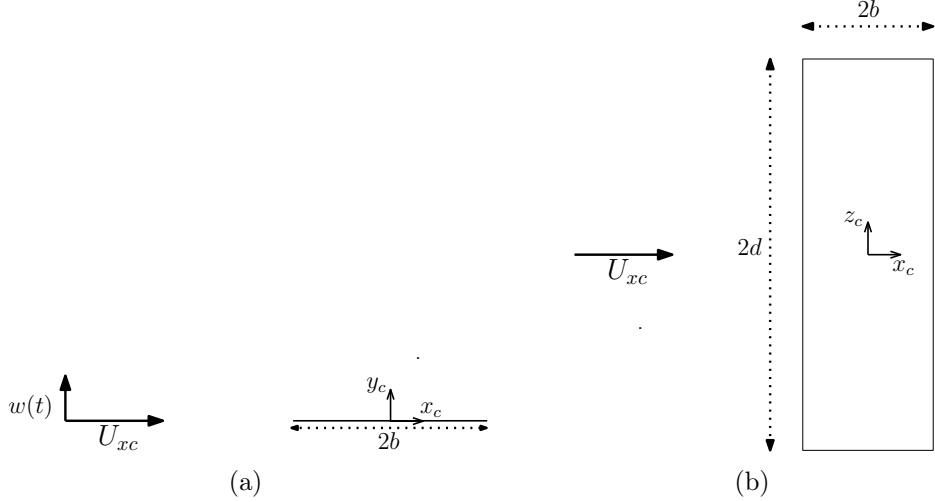


Figure 4: Amiet's model configuration. (a) Unwrapped strip, (b) 3D view of an isolated vane with the corresponding impinging flow.

velocity fluctuations. In the present implementation, the pressure jump of each vane is computed on several radii assuming a wake-to-wake correlation for the impinging turbulence statistics, which is consistent with the azimuthal periodicity of the configuration. This approach can be compared to the one adopted by de Gouvillie [62], in the context of incident turbulence noise, and by Joseph and Parry [63] for the noise resulting from the interaction of a boundary layer with a stator. Moreover, the present Amiet's blade response includes the effect of sub-critical gusts since they have a significant impact at low and moderate frequencies as observed by Moreau *et al.* [12]. The pressure jump on each vane can then be used as an equivalent dipole source distribution in the framework of Goldstein's acoustic analogy for annular ducts to obtain the upstream and downstream SWL.

2.3. Model of Ventres

In the first version of the model of Ventres *et al.* [32], the impinging flow and the cascade response are both two-dimensional. An **upwash** velocity fluctuation normal to the chord of the vane is considered. Let w be such a gust, of pulsation ω and impinging on the vane number ν . w is written as follows:

$$w(x_c + \nu d, y_c + \nu h) = w_0 e^{-i\omega t} e^{i(k_{x_c}(x_c + \nu d) + k_{y_c}(y_c + \nu h))}, \quad (4)$$

where k_{x_c} and k_{y_c} are the wave numbers along the directions x_c and y_c respectively. Figure 5 shows a typical unwrapped strip in the configuration of Ventres. The vane cascade is immersed in an **inviscid** uniform mean flow with zero angle of attack, the components of which are $(U_{x_c}, 0, 0)$.

In order to ensure the **slip** condition on the flat plate, a velocity field is produced by the impingement of the incident fluctuation. From the momentum and the continuity equations verified by the acoustic pressure, Ventres *et al.* [32] show that the problem is reduced to solving the following integral equation:

$$w(x_c + \nu d, y_c + \nu h) = \int_{-c/2}^{c/2} K_c(x_c - x', y_c) \frac{\Delta p_0(x') e^{i\nu\sigma}}{\rho_0 U_{x_c}} \frac{dx'}{c/2}, \quad (5)$$

where

$$\sigma = k_{x_c} d + k_{y_c} h, \quad (6)$$

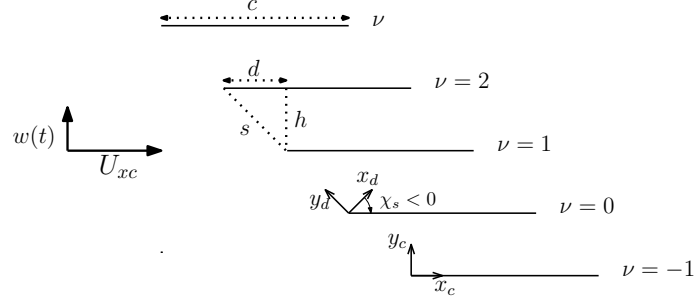


Figure 5: Unwrapped strip for the model of Ventres.

is the interblade phase angle. $\Delta p_0(x')$ is the unsteady pressure jump across the vane $\nu = 0$ and K_c corresponds to the kernel function of the problem which accounts for the cascade as defined in [32]. This equation is numerically solved by a collocation method. After obtaining the unsteady loading on every vane at each radius, the strips are wrapped back to their initial cylindrical form. The loading is then used as a dipole source in the acoustic analogy of Goldstein [extended to annular ducts](#) (see Eq. (5a) in [34]) which gives the acoustic field within an infinite annular duct with a uniform axial mean flow.

2.4. Models based on Glegg's cascade response

Glegg [45] developed a cascade response for a vane cascade of infinite span. Contrary to the cascade response of Ventres *et al.* [32], [the upstream disturbance is modeled as a 3D gust](#). This means that the wavenumber along z_c (k_{z_c}) is no longer equal to zero, allowing for a [more representative](#) description of the physical phenomena. Additionally, the z-component of the mean velocity U_{z_c} can be taken into account and is equivalent to consider a swept stator vane (see Figs. 6a and 6b). Glegg considers an incident gust which is assumed to be a harmonic wave written as follows:

$$w(x_c, y_c, z_c) = w_0 e^{-i\omega t} e^{i(k_{x_c} x_c + k_{y_c} y_c + k_{z_c} z_c)}, \quad (7)$$

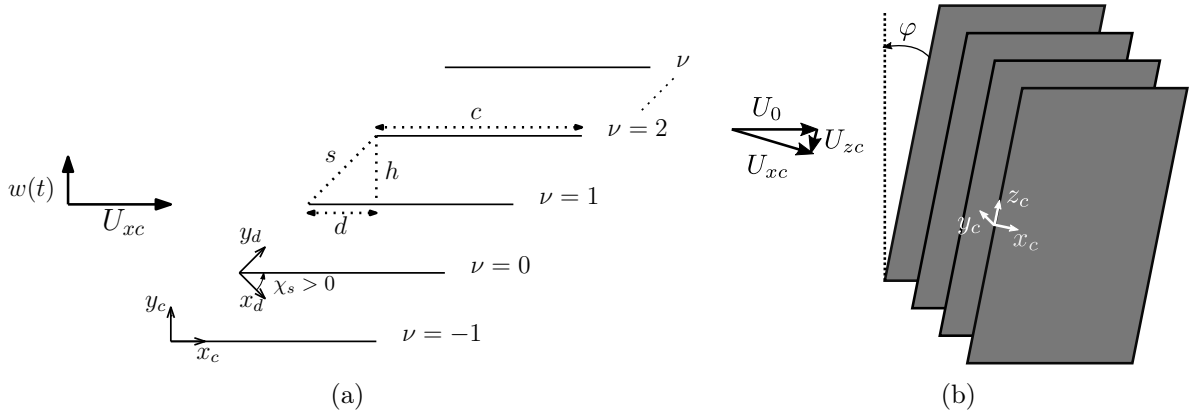


Figure 6: Glegg's model configuration. (a) Unwrapped strip, (b) 3D view of a vane cascade with a sweep angle φ and the corresponding impinging flow.

Similarly to the model of Ventres *et al.* [32], the objective is to determine the velocity, and more precisely in this case its potential ϕ , produced by the impingement of the gust in order to ensure the no-slip condition on the flat-plate. It follows that for each vane, the incident gusts have an identical amplitude relative to the leading-edge, but will be shifted in phase by the same inter-blade angle as defined in equation (6). This also applies to the vane response.

Considering this and the fact that the vanes and their [respective](#) wake introduce a discontinuity in the potential field, the potential jump across the vane ν and its wake can be written as the delayed potential jump across the vane as follows:

$$\Delta\phi_\nu(x_c, z_c, t) = \Delta\phi_0(x_c - \nu d)e^{-i\omega t + i(\nu\sigma + k_{zc}z_c)}. \quad (8)$$

Since the vanes have an infinite span, the model cannot predict the dispersion of the spanwise wavenumber, which means that k_{zc} is conserved in the cascade response. From the continuity and momentum equations, the integral equation of the velocity potential can be deduced:

$$\phi(x_c, y_c) = \frac{1}{2\pi} \int_{-\infty}^{+\infty} \int_{-\infty}^{+\infty} \frac{-i\epsilon D(\eta)}{(\omega - k_{zc}U_{zc} + \eta U)^2/c_0^2 - \eta^2 - \epsilon^2 - k_{zc}^2} \left[\sum_{\nu=0}^{V-1} e^{i\nu(\sigma + \eta d + \epsilon h)} \right] e^{-i\eta x_c - i\epsilon y_c} d\eta d\epsilon, \quad (9)$$

where $U = \sqrt{U_{xc}^2 + U_{zc}^2}$ is the velocity magnitude, V the number of vanes and $D(\eta)$ the Fourier transform of the potential jump across the vane number 0:

$$D(\eta) = \frac{1}{2\pi} \int_0^{+\infty} \Delta\phi_0(x_c) e^{-i\eta x_c} dx_c. \quad (10)$$

Glegg solves the integral Eq. (9) using the Wiener-Hopf technique with the following boundary conditions:

- (a) the velocity potential must be continuous upstream of the vanes:

$$\Delta\phi(x_c, nh, z_c, t) = 0, \quad \forall x_c < nd, \quad \forall (z_c, t) \in \mathbb{R}^2 \text{ and } \forall n \in \mathbb{Z}. \quad (11)$$

- (b) the total velocity normal to the plate must be zero ([slip](#) condition):

$$(\vec{w} + \vec{u}) \cdot \vec{u}_{y_c} = 0 \Rightarrow w + \frac{\partial\phi}{\partial y_c} = 0, \forall ld < x_c < ld + c, y_c = lh, \forall (z_c, t) \in \mathbb{R}^2 \text{ and } \forall l \in \mathbb{Z}. \quad (12)$$

- (c) the pressure must be continuous at the TE (Kutta condition [59]) and in the wake:

$$\Delta p(x_c, nh, z_c, t) = 0, \quad \forall x_c \geq c + nd, \quad \forall (z_c, t) \in \mathbb{R}^2 \text{ and } \forall n \in \mathbb{Z}, \quad (13)$$

where $p = -\rho_0 D\phi/Dt$.

Solving Eq. (9) requires to decompose the potential and the potential jump into four parts:

$$\phi_0 = \phi_0^1 + \phi_0^2 + \phi_0^3 + \phi_0^4, \quad (14)$$

$$\Delta\phi_0 = \Delta\phi_0^1 + \Delta\phi_0^2 + \Delta\phi_0^3 + \Delta\phi_0^4. \quad (15)$$

Each term is the solution of a specific problem with its own boundary conditions. The first term is the solution of a vortical gust impinging a cascade of flat-plates with a LE and a semi-infinite chord; boundary conditions (a) and (b) are considered in this first problem. The second part considers a cascade of flat-plates of semi-infinite chord with a TE, interacting with the field ϕ_0^1 obtained by solving the first problem; this problem is subject to boundary conditions (b) and (c). However, solving this second step introduces a new potential ϕ_0^2 which modifies the upstream part of the problem. This results in an acoustic field which does not satisfy the boundary condition (a). Two additional solutions, which are coupled, need to be introduced: ϕ_0^3

solution of the first problem but taking ϕ_0^2 and ϕ_0^4 into account, and ϕ_0^4 solution of the second problem but taking ϕ_0^3 into account. Obtaining an exact solution through the coupling of the last two steps requires to solve an infinite matrix system. As a consequence, the solution of the problem can only be approximated by truncating this system. In Posson's model, which is an extension of Glegg's model (see section 2.4.2), the extrapolation of Richardson [64] proposed by Majumdar and Peake [65] has been used in order to reduce the computational cost of the prediction and ensure a converged solution. In the present application of this model, around 2000 terms had to be computed to get a converged solution.

Once the potential jump on the flat plates is obtained, Glegg [45] gives an explicit formula of the scattered velocity potential outside of the cascade resulting from the impingement of the incident gust. It is expressed as the sum of acoustic modes of index k scattered by the cascade:

$$\phi^\pm(\mathbf{x}, t) = \pm \frac{\pi w_0 C^2}{\beta s_e} \sum_{k=-\infty}^{\infty} \pm \frac{\zeta_k^\pm D(\lambda_k^\pm)}{\sqrt{\kappa_e^2 - f_k^2}} e^{i[-\lambda_k^\pm(x_c - y_c d/h) + (\sigma - 2\pi k)y_c/h + k_{zc}z_c]} e^{-i\omega t}, \quad (16)$$

with:

$$\begin{aligned} M &= U/c_0 & \beta &= \sqrt{1 - M^2} & \omega_g &= \omega - k_{zc}U_{zc} \\ s_e &= \sqrt{d^2 + \beta^2 h^2} & \tan \chi_e &= d/\beta h & \lambda_k^\pm &= \kappa M + \eta_k^\pm \\ \zeta_k^\pm &= \beta \sqrt{\kappa_e^2 - (\eta_k^\pm)^2} & \kappa_e^2 &= \kappa^2 - (k_{zc}/\beta)^2 & \kappa &= \omega_g/(c_0 \beta^2) \\ \eta_k^\pm &= -f_k \sin \chi_e \pm \cos \chi_e \sqrt{\kappa_e^2 - f_k^2} & f_k &= (\sigma - 2\pi k + \kappa M d)/s_e \end{aligned}$$

In practice, this infinite sum is reduced to the cut-on modes. Indeed, the mode k propagates only if it satisfies the cut-on criterion $\kappa_e^2 - f_k^2 > 0$. It should also be noted that the acoustic field is obtained without explicitly making use of the distribution of the acoustic sources on the vanes. This dramatically reduces the computational cost of such a method in comparison to annular models. This particular feature has been kept by Hanson when extending Glegg's cascade response, as explained in the following section.

2.4.1. Hanson's model

Hanson's model [3, 57] is based on Glegg's cascade model. The main advance of Hanson's approach is the ability to model more realistically the impinging flow by taking into account the in-homogeneity and the anisotropy that characterize the flow in the interstage. Hanson also developed the formalism to change the coordinate system by successive rotations in order to take into account the specific features of complex blade geometries (variable stagger, sweep and lean angles as shown in Figs. 7a and 7b). Moreover, Hanson adapted Glegg's model to a cylindrical system which allowed him to consider the wavenumbers in the duct coordinate system with the actual number of blades and vanes. Hanson's model also resorts to the strip theory: the geometry is divided into several cylindrical cuts of thickness Δr . For each strip, the acoustic power is then computed and radiated only within the considered Δr strip using Glegg's approach. This method differs from the approach of Ventres and Posson since the pressure jump is not computed and the computation of the acoustic power is not correlated between two different radii. Finally, in Hanson's model, only a free-field propagation is considered which means that there is no energy distribution over the duct acoustic modes.

Despite these two limiting assumptions, this model predicts the shapes and levels of the acoustic power spectra fairly correctly [66]. Additionally, the fact that the model does not consider an in-duct propagation reduces significantly its computational cost. This can be a particularly interesting asset, especially for parametric studies in an industrial context.

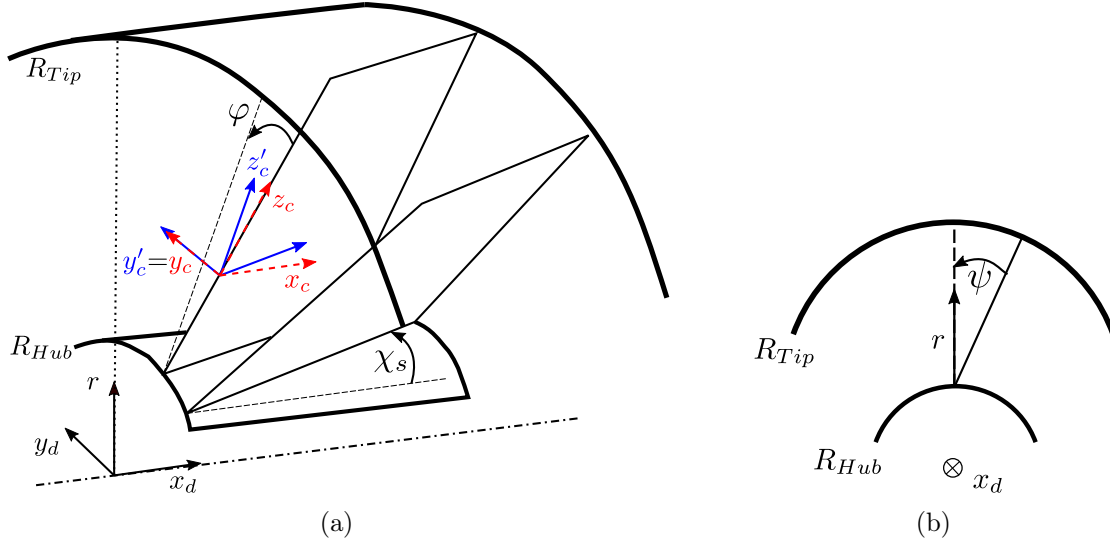


Figure 7: Introduction of the sweep angle φ and the lean angle ψ as proposed by Hanson. (x'_c, y'_c, z'_c) is the reference frame before the sweep angle rotation, which leads to the reference frame (x_c, y_c, z_c) . (a) 3D view, (b) Front view.

2.4.2. Posson's model

Posson's model [47, 48, 34] includes Hanson's developments allowing to account for complex geometrical features and also resorts to the strip theory: each strip corresponds to Glegg's configuration in which a rectilinear cascade of zero-thickness flat plates of infinite span is subject to a 3D impinging gust. However, Posson extended Glegg's model in order to compute both the acoustic field in the inter-blade domain and the unsteady pressure jump across the vanes. By solving equation (9), the latter eventually leads to the pressure distribution along the chord which can be considered as an equivalent dipole source distributed on the vane surface once the cascade has been wrapped back to its initial position. The vane cascade responses subject to each gust are then added up to obtain the source distribution corresponding to the real impinging flow. These sources are finally radiated through the duct using the generalized Goldstein acoustic analogy [59]. The use of a linear cascade response in conjunction with an annular propagation is responsible for some issues already identified by Posson *et al.* [47]. One of them is the non-coincidence of the cut-off frequencies of the duct-modes with that of the linear cascade which results in unphysical resonances. In order to tackle this issue, a first correction has been implemented in the model and validated on a test-case [34]. In the present case, this annular correction, which only works for unswept vanes, is not taken into account since the vane sweep angle is not negligible. In order to reduce these unphysical resonances, the studied frequencies in the following sections have been selected in order to avoid the duct **cut-off** frequencies, following suggestions by Grace [40, 38].

2.4.3. Masson's model

Masson *et al.* [49] extended Posson's model by taking into account the swirling motion of the fluid. This model uses Posson's cascade response as a dipole source distribution in the generalized Green's function developed by Posson and Peake [50] for homentropic flows, which propagates the sound in an annular duct considering a swirling and sheared mean flow. Such an approach **is more representative of the interstage 3D unsteady flow** with respect to models relying only on Goldstein's analogy, but simultaneously increases the **level of complexity of the model** since an analytical expression cannot be derived for the Green's function any longer. As the swirl of the flow is only significant upstream of the stator, in the interstage, only an assessment of the upstream sound power level (SWL) is performed in the present study. This also implies that the non-acoustic modes resulting from the presence of the swirling flow, such as the nearly-convected

modes or the critical layer, are not taken into account since they only propagate downstream [67].

In the following sections, these models are all applied to the NASA Source Diagnostic Test configuration and, for the first time, directly compared to each other. Their specific features are highlighted and the impact of their respective assumptions on the noise predictions is evaluated. Their sensitivity to the variation of some parameters mentioned in the four previously described building blocks is also investigated.

3. Test case: the NASA SDT fan rig

All the models are assessed on the NASA Source Diagnostic Test (SDT) case that has become an AIAA benchmark for fan broadband noise predictions since 2015.

3.1. Experimental set-up

In the framework of the NASA advanced Subsonic Technology Noise Reduction Program, a series of experiments were performed on the 22-in SDT fan rig of the NASA Glenn low-speed wind tunnel. One of the main objectives of this project was to identify and characterize the broadband noise sources in a modern high-bypass-ratio turbofan engine for different flight conditions: approach, cut-back and fly-over. The interaction noise was part of the main mechanisms that were studied during these experiments. Far-field noise measurements were performed upstream and downstream of the fan stage along with hot-wire measurements in the interstage, providing both flow fields and acoustic power at these positions. Azimuthal mode detection rings were also installed in the interstage.

The SDT fan stage is representative of a 1/5th scale of a modern high bypass ratio (HBR) turbofan engine. It consists of a 22-bladed rotor and a variable number of Outlet Guide Vanes (OGV). Three different stage configurations have been tested: the baseline geometry composed of 54 vanes, the low-count geometry with 26 vanes, and the low-noise geometry composed of 26 swept vanes (see Fig. 8). These three stators have the same solidity, resulting in an increased chord for the low-count and low-noise configurations. They all display a constant chord along the span.

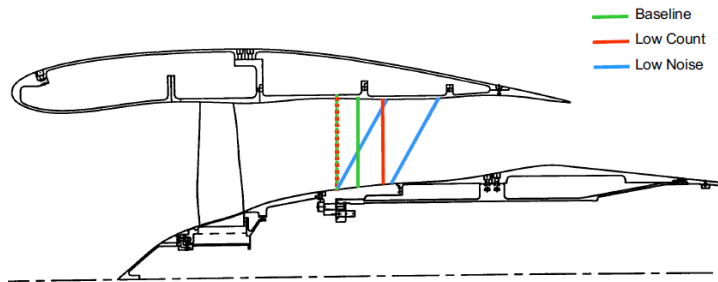


Figure 8: SDT stage configurations.

In the present study, the aforementioned models are only assessed at approach conditions on the baseline configuration, the main characteristics of which are listed in Table 1:

R_{Hub} at OGV LE (m)	R_{Tip} at OGV LE (m)	Ω (rpm)	Vane chord (m)
0.1397	0.2794	7808	0.040

Table 1: Main parameters of the SDT baseline configuration.

The description of the test campaign as well as the main aerodynamic and acoustic experimental results can be found in [68, 69, 70, 71, 72, 73]. The noise measurements used as a reference in the following sections correspond to the upstream and downstream **far-field** measurements of the total broadband noise, from which the rotor noise was subtracted. As a consequence, the experimental noise spectra theoretically **correspond** only to the noise produced by the stator, which includes the RSI noise.

3.2. CFD computations

In the present study, the input parameters of the models are retrieved from two different RANS simulations. The first one is a 3D viscous mixing-plane simulation performed by Nallasamy and Envia in 2005 [36] using the code APNASA. A modified $k - \epsilon$ turbulence model [74] was used to account for the effect of turbulence. The mesh is composed of about one million cells: 407 cells in the streamwise direction, and 51 cells in both azimuthal and radial directions. The second was performed by Leonard *et al.* in 2016 [66] as part of a comprehensive numerical study on the SDT configuration, involving both RANS and LES simulations. The simulation was performed using the ANSYS CFX v15.0 solver. Similarly to the previous simulation, a mixing-plane was used at the rotor-stator interface. In this case the $k - \omega$ SST model was used to simulate the turbulent behavior of the flow. The mesh is a hybrid unstructured grid composed of prism cells on walls, to accurately resolve the boundary layer, and of tetrahedral cells in the rest of the domain. It is composed of 75 million cells in total. The dimensionless wall-normal distance y^+ of the first cell was maintained under 50.

Figure 9 displays the radial evolution at the stator LE of the main model input parameters: the absolute Mach number (Fig. 9a), the axial Mach number (Fig. 9b), the turbulence intensity (TI) in the background flow (Fig. 9c) and in the wake (Fig. 9d), as well as the turbulence length scale (Fig. 9e). Leonard *et al.* [66] computed the integral length scale Λ using the wake width:

$$\Lambda = 0.21L_w \quad (17)$$

where L_w is the wake width, whereas Nallasamy and Envia [36] computed it using the k and ϵ variable of the $k - \epsilon$ turbulence model:

$$\Lambda = C_\mu \frac{\bar{k}^{3/2}}{\bar{\epsilon}} \quad (18)$$

where $C_\mu = 0.09$, and \bar{k} and $\bar{\epsilon}$ are the circumferentially averaged turbulence kinetic energy and dissipation computed from the RANS solution.

Leonard *et al.*'s RANS is in very good agreement with the measurements but displays a slight underestimation of the background and wake TI. Nallasamy and Envia's RANS displays larger disparities with the measurements, especially regarding the wake TI for which the underestimation is larger than that observed with Leonard *et al.*'s RANS. The overall shape of the profiles is well recovered by both simulations. The integral length scale profiles however display different trends close to the casing, which may also have an impact on the noise predictions [75].

All the following acoustic predictions are performed using data retrieved from Leonard *et al.*'s RANS simulation, which shows the best agreement with the measurements, except in Section 4.2.1 in which predictions relying on both simulations are explicitly compared, and in Appendix A in which Nallasamy and Envia's RANS data are used to check the convergence of Ventres' cascade response. Nallasamy and Envia's RANS is only used as a tool to assess the impact of mean flow variations and will not be used to perform comparisons with the measurements.

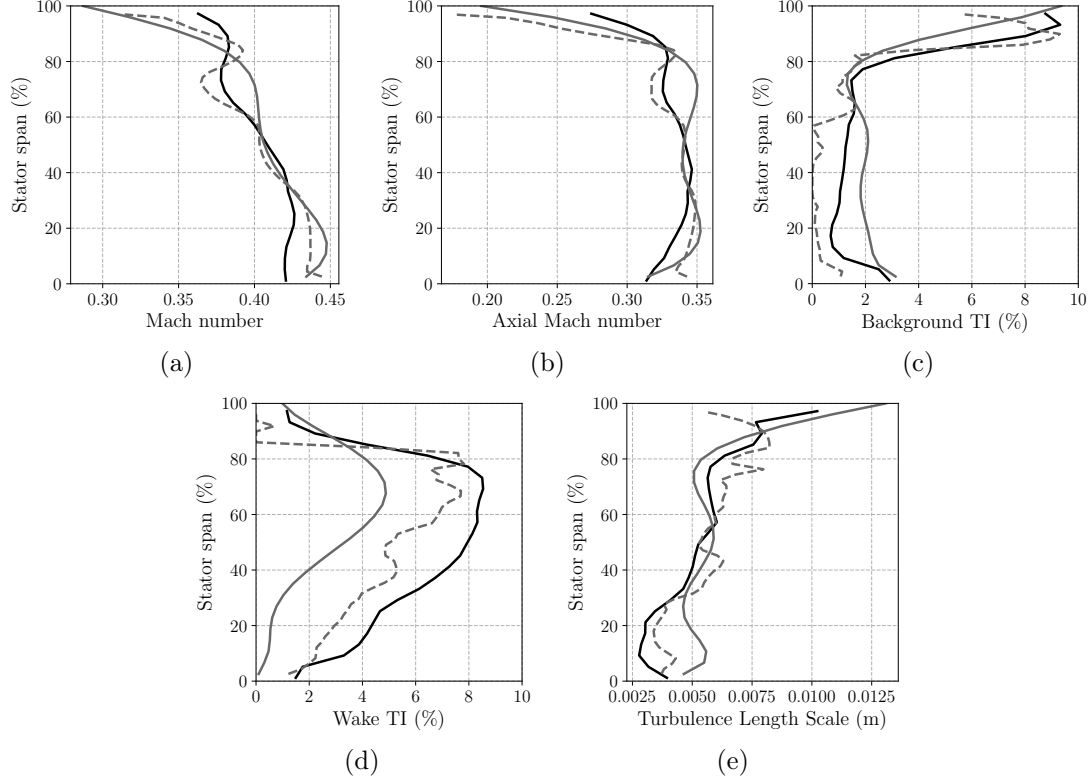


Figure 9: Comparison of the model input parameter extractions performed on two different RANS simulations. Experiment (—), Nallasamy and Envia’s RANS (---), Leonard *et al.*’s RANS (· · ·). (a) Mach number, (b) Axial Mach number, (c) Background turbulence intensity, (d) Wake turbulence intensity, (e) Turbulence length scale.

4. Sensitivity Study

This section is dedicated to the parametric study of the models introduced in Section 2.1. It aims at determining if some assumptions made in the development of the models are responsible for a lack of representativeness of the configuration. The objective of this study is also to highlight and characterize the impact of variations in the input parameters on the broadband noise predictions.

In the following section, Ventres’ model implementation is based on the original model of Ventres *et al.* [32] extended with additional developments from Nallasamy and Envia [36] regarding the turbulence spectrum, which enables to consider both the background and wake components of the impinging flow. The latter feature is implemented by default in the models of Posson [47, 48, 34], Masson [49], Hanson [3, 57] and Amiet [10, 11, 12, 13]. If not clearly mentioned, the turbulence state of the incident flow is modeled using the Liepmann isotropic spectrum.

4.1. Geometry definition

In the case of a fan stage, thin and moderately cambered profiles, with small angles of attack and small impinging perturbations are studied. These parameters ensure that the unsteady loading is hardly depending on geometric parameters [76] and, consequently, that the zero thickness flat plate approximation is a fairly justified assumption. The OGVs also display a substantial number of vanes with a significant overlapping. This implies that the response of the vane depends on its surrounding and therefore that the cascade effect cannot be neglected (as seen in section 4.3). One parameter that significantly determines the cascade effect is the stagger

angle of the vanes [60]. Hence, the stagger angle of the equivalent flat plate geometry must be chosen **carefully** in order to faithfully transpose the actual vane behavior. The first intuitive choice is to set the stagger angle with respect to the chord line (noted χ_{geo} in Figure 10).

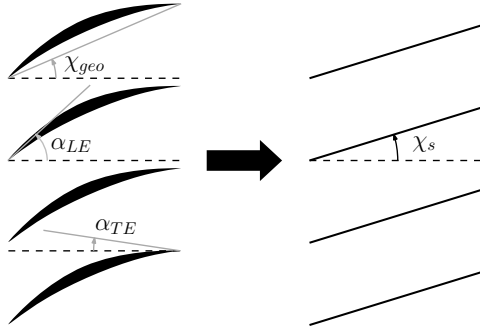


Figure 10: Equivalent flat plate geometry.

Grace *et al.* [37, 38] for instance suggested another option to select the stagger angle, which takes the camber at the LE α_{LE} and at the TE α_{TE} into account. This weighted stagger angle is computed using the following relationship:

$$\chi_s = A \alpha_{LE} + B \alpha_{TE}. \quad (19)$$

Figures 11, 12 and 13 show the SWL obtained from Hanson's, Posson's, and Masson's models respectively. Two weighting configurations are compared against the geometry using χ_{geo} : $(A, B) = (0.5, 0.5)$ (noted $A50B50$) and $(A, B) = (0.9, 0.1)$ (noted $A90B10$). The $A90B10$ configuration corresponds to the highest stagger angle, while the χ_{geo} configuration corresponds to the lowest.

For Hanson's model (Fig. 11), the χ_{geo} -configuration gives the lowest noise levels both upstream and downstream of the stator. The highest noise levels, however, are obtained for the $A90B10$ -configuration. The SWL of the $A50B50$ -configuration lies in between the two others but is closer to the χ_{geo} -configuration, especially for the exhaust prediction, for which the levels are almost identical, and at high frequency for the upstream prediction. Downstream of the stator, a maximum gap of 2 dB is observed between the $A90B10$ and the χ_{geo} configurations. The $A50B50$ -configuration gives quite similar results as the χ_{geo} configuration on the studied range of frequency. The gap between the $A90B10$ -configuration and the two others progressively decreases until the curves are superimposed for frequencies higher than 14 kHz. The most noticeable changes are observed upstream of the stator where the gap between the configurations $A90B10$ and χ_{geo} can reach values up to 4.5 dB. From 1 kHz up to 8 kHz, this gap is of 3.8 dB on average and decreases progressively until it reaches a constant value of 1.3 dB. The noise levels obtained from the $A50B50$ -configuration are between those of the two others, the gap with the χ_{geo} -configuration being smaller than with the $A90B10$ configuration. At very high frequency, the $A50B50$ and the χ_{geo} configurations give quite similar results. Even though the three curves **do not overlap** at high frequency, as with the downstream predictions, the slopes of all spectra are almost identical, indicating a similar behavior.

The same comments can be made for the results obtained with Posson's model (see Fig. 12). Indeed, they display the same trends relatively to the stagger angle variation except at very high **frequencies** for which the curves do not overlap.

Masson's model, however, displays a much different behavior than the two previous models (see Fig. 13). Indeed, the modification of the stagger angle has almost no effect at low frequencies, whereas a small effect is observed at high frequencies, the highest levels being obtained with the lowest stagger angle. This unexpected result actually stems from the effect of the swirl on

the amplitude of the cut-on modes as shown in Fig. 14. At low frequencies, the increase in stagger angle induces an increase in the **co-rotating mode amplitudes with a negative azimuthal order** that almost balances the decrease in amplitude of the low frequency contra-rotating modes (positive azimuthal order), which results in a global radiated noise that remains unchanged. At high frequencies, however, a decrease in the contra-rotating mode amplitudes is observed whereas the co-rotating mode amplitudes remain almost the same, which explains the lower noise levels observed at high frequencies as the stagger is increased. In the case of Posson’s model (see Fig. 15), no low-frequency balancing of the mode amplitudes is observed: the amplitude increase observed for the co-rotating mode is much more intense than the decrease in contra-rotating mode amplitudes, resulting in higher noise levels at low frequencies as the stagger angle is increased. Additionally, the impact of the stagger angle on the modal amplitudes at high frequencies is marginal, which explains the similar high frequency noise levels for all Posson’s predictions. As a consequence, the swirl tends to reduce the stagger angle effect at low frequencies but enhances it at high frequencies. **Regardless of the stagger angle, Figs. 14 and 15 reveal that the presence of the swirl moves the “V” shape of the cut-on axis towards the positive azimuthal orders, which in the present case correspond to contra-rotating modes).** Such an asymmetry was also observed by Premo and Joppa [77] when analyzing the azimuthal mode decomposition performed in the interstage of the NASA SDT. Premo and Joppa [77] also observed higher levels for the co-rotating modes, which is well recovered by both Posson’s and Masson’s models. Figure 16, which shows the SWL difference between Posson’s and Masson’s model predictions for each value of stagger angle, also reveals that the effect of the swirl increases when the stagger angle is increased, since the predictions of both models are much closer for low stagger angle values. This is due to the fact that the increase in the stagger angle leads to an increase in the amplitude of the co-rotating modes, which tends to be cut-off because of the swirl effect.

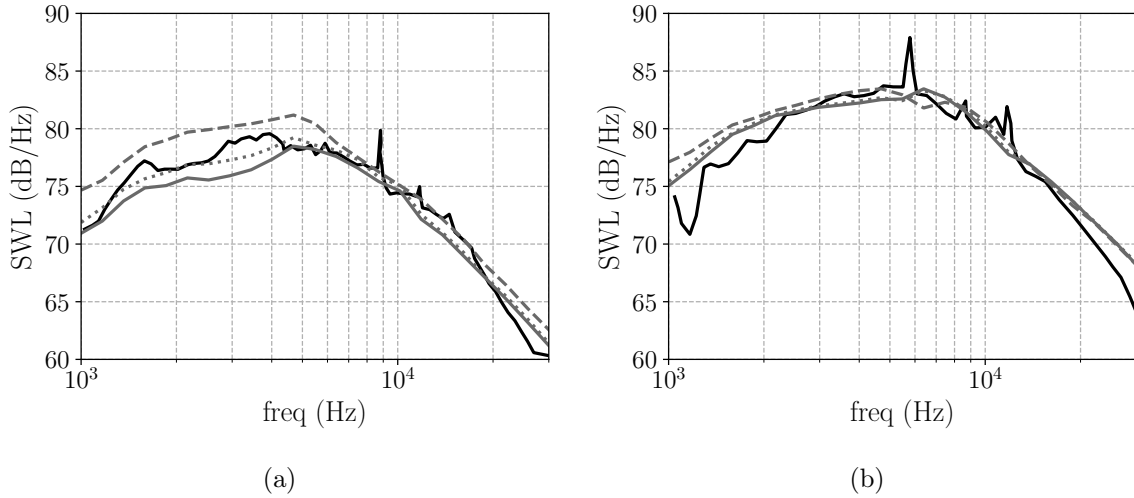


Figure 11: Stagger angle effect, Hanson’s model. Experiment (—), χ_{geo} (—), χ_{A50B50} (·····), χ_{A90B10} (- - -). (a) Upstream SWL, (b) Downstream SWL.

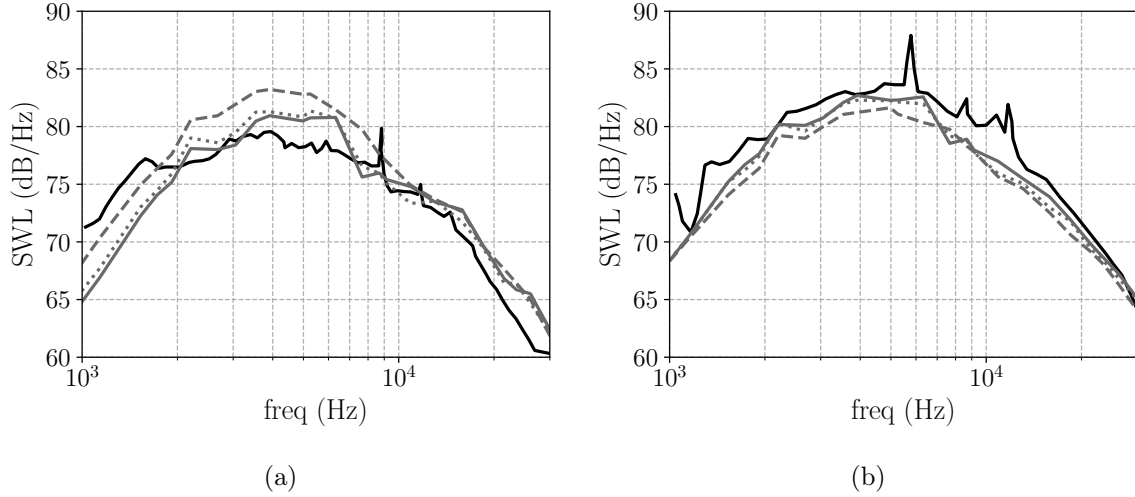


Figure 12: Stagger angle effect, Posson's model. Experiment (—), χ_{geo} (—), χ_{A50B50} (····), χ_{A90B10} (- · - ·). (a) Upstream SWL, (b) Downstream SWL.

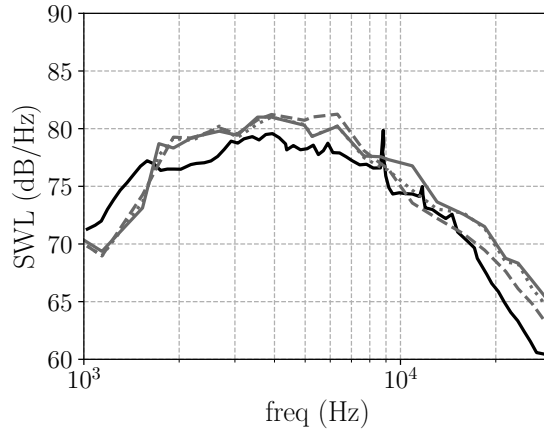


Figure 13: Stagger angle effect, Masson's model. Experiment (—), χ_{geo} (—), χ_{A50B50} (····), χ_{A90B10} (- · - ·). Upstream SWL.

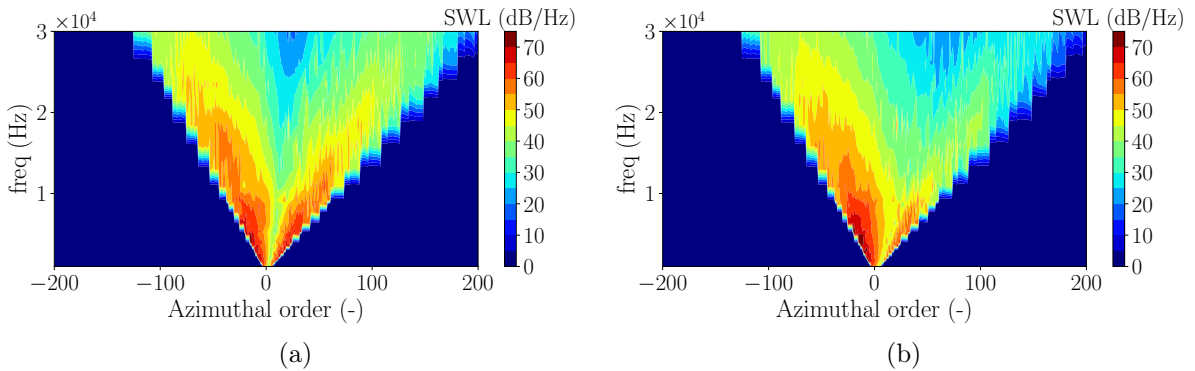


Figure 14: Upstream modal amplitude for different stagger angles, Masson's model. (a) χ_{A50B50} , (b) χ_{A90B10} .

These changes not only result from the modification of the stagger angle, but also from the induced modification of the stator solidity. However, as pointed out by Hanson, solidity variations at constant vane count have a very limited impact on the radiated SWL [46]. This implies that

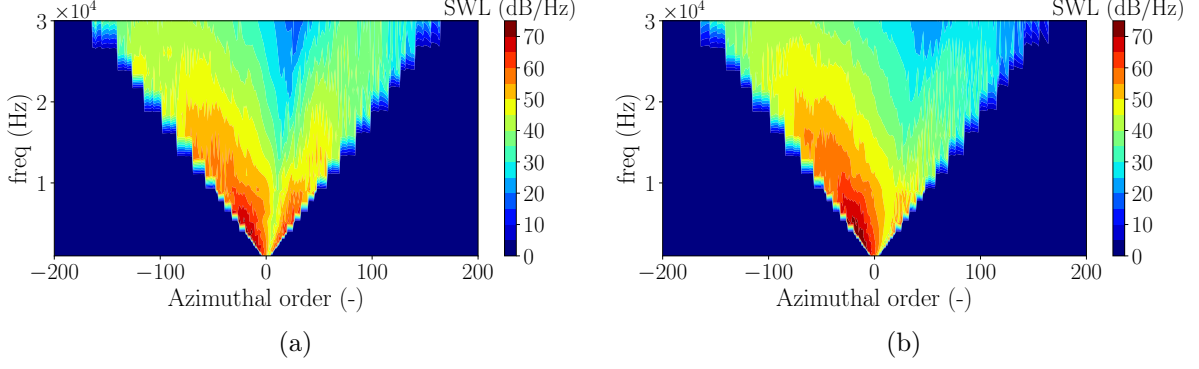


Figure 15: Upstream modal amplitude for different stagger angles, Posson’s model. (a) χ_{A50B50} , (b) χ_{A90B10} .

most of the modifications observed in the present study can be attributed to the modification of the stagger angle itself. Posson also studied the impact of the modification of the stagger angle at constant solidity for an unwrapped vane cascade subject to particular harmonic gusts [78]. Posson observed that an increase in the stagger angle induces a decrease in the downstream SWL, especially at low frequencies. The upstream SWL, however, is weakly impacted by such a modification since only a slight increase in the SWL can be observed when the stagger angle is increased. This is also consistent with the results from Blandeau *et al.* [79] and Gea-Aguilera *et al.* [80]. As it can be seen from the present study, this behavior is partially recovered but with discrepancies that are significantly larger than those observed by Posson. Considering a complete 3D vane row and integrating turbulence over a broad range of wavenumbers seems to intensify the impact of such modifications. As a consequence, the behavior of such models on a real geometry cannot be thoroughly assessed or anticipated only by studying particular harmonic gusts on an unwrapped vane row. This might be due to the fact that increasing the stagger angle exposes an increasing part of the suction side LE to the open flow : the waves are more easily scattered back into the interstage and less prone to downstream radiation across the cascade. According to scattering theory [81], for low frequencies, that is, large wave numbers, this trend is even more pronounced and explains the results observed both at the intake and at the exhaust. It should however be kept in mind, that the rotor also filters the sound waves from the OGV, which is not taken into account in the present models.

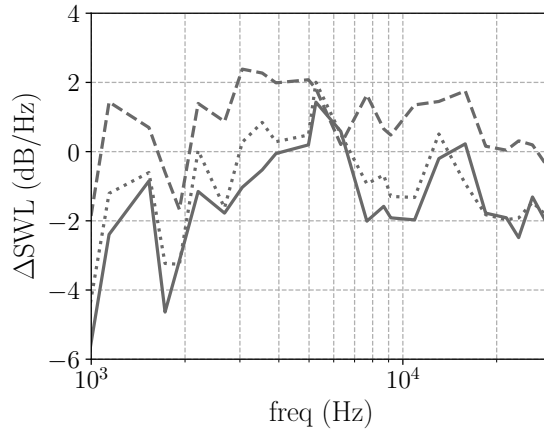


Figure 16: SWL difference between Posson and Masson’s models for different stagger angle values. χ_{geo} (—), χ_{A50B50} (⋯⋯), χ_{A90B10} (---). Upstream Δ SWL.

Given that the RSI mechanism is mainly a LE phenomenon, the A90B10 configuration has

been selected as the default stagger angle for the following sections, even though it does not produce the results which are the closest to the experimental data. Note that given the screen effect of the fan rotor is not accounted for, higher predicted levels should be expected upstream and lower downstream, as shown by Blázquez-Navarro & Corral [82] and Ying *et al.* [83].

4.2. Impinging flow definition

4.2.1. Sensitivity to modifications of the mean flow characteristics

The mean flow parameter computation through RANS simulations is a determinant step. In particular, the structure of the rotor wakes is remarkably sensitive to the mesh refinements on the rotor blades, to the mesh refinements in the wake, and to the chosen turbulence model. Indeed, wall refinements as well as the turbulence model have a major impact on the simulation of flow separations that govern the structure of the wake downstream of the TE. A very fine mesh is also required in the wake in order to correctly transport it down to the mixing plane and to get a good estimate of the turbulence intensity and integral length scale within it. Too coarse a mesh would diffuse the wake and dampen the turbulence intensity. Figures 17 and 18 show the noise predictions obtained with Hanson’s and Posson’s models, respectively, using the two different RANS inputs presented in section 3.2.

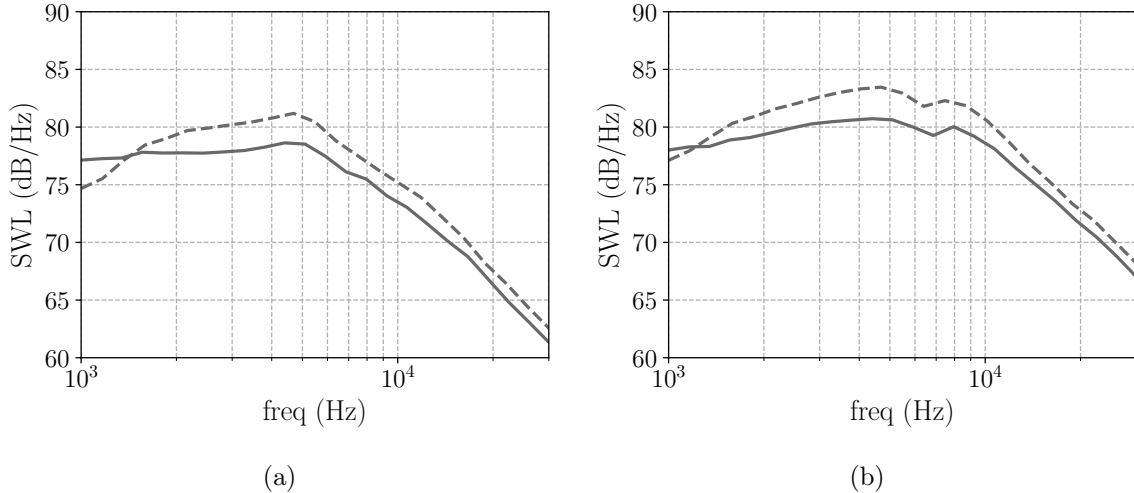


Figure 17: Mean flow variation effect, Hanson’s model. Nallasamy and Envia’s RANS (—), Leonard *et al.*’s RANS (---). (a) Upstream SWL, (b) Downstream SWL.

As it can be seen, the use of different data sets as input parameters for the models (see Section 3.2) has a significant effect on the noise predictions, regarding both the absolute noise levels and the shape of the spectra. The higher wake turbulence intensity from Leonard *et al.*’s RANS simulation [66] is responsible for an increase in the predicted noise at medium frequencies of 2 to 3 dB for both Hanson’s (Fig. 17) and Posson’s (Fig. 18) models, whether it is for the upstream or the downstream noise. A slight increase in the noise at high frequencies can be observed for the predictions using Hanson’s model. Additionally, the smaller integral length scale near the casing in Leonard *et al.*’s RANS (Fig. 9e) seems to be responsible for a decrease in the predicted noise at low frequencies. Indeed, as pointed out by Lewis *et al.* [75] in their study on the different estimates of the integral length scale, larger turbulent structures near the casing (shown in Fig. 9e) lead to an increase in the noise at low frequencies which is consistent with an increased noise when using Nallasamy and Envia’s data set. Similar results have been obtained by Grace [84].

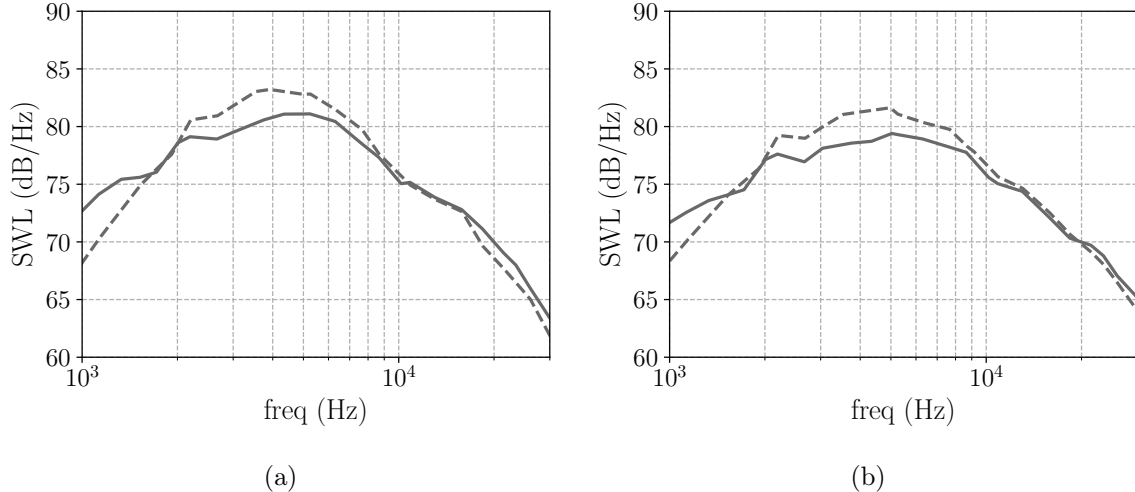


Figure 18: Mean flow variation effect, Posson's model. Nallasamy and Envia's RANS (—), Leonard *et al.*'s RANS (- - -). (a) Upstream SWL, (b) Downstream SWL.

4.2.2. Difference between 2D and 3D models

As stated in Section 2.1, analytical models using the cascade approach can be split into two categories: on the one hand, there are the 2D models, which consider a wave vector in the (x_c, y_c) plane in the cascade reference frame to model the impinging flow and the cascade response. On the other hand, there are the 3D models, which consider a third wave number component k_{zc} in the spanwise direction.

The aim of this section is to assess the impact of the spanwise wave number on the noise prediction. To do so, the 3D model of Posson [47, 48, 34] is compared to the 2D model of Ventres *et al.* [32].

In order to get reliable comparisons, two points need to be addressed. Firstly, the kernel function in Ventres *et al.*'s model is computed using a semi-analytic method contrary to that of Posson's model that is obtained analytically. As a consequence, the convergence of Ventres' cascade response needs to be ensured before any comparison with the 3D model of Posson. To this aim, the 2D cascade response of Posson has been implemented in the model of Ventres, while keeping the other characteristics of the code such as the 2D anisotropic turbulent spectrum introduced by Nallasamy and Envia [36], and has been directly compared to the noise predictions obtained from Ventres' model. This convergence study is presented in detail in Appendix A and shows almost identical results between Ventres' model with 500 *chordwise* discretization points and the 2D Posson model, which ensures reliable predictions using Ventres' model.

Secondly, Ventres' model was originally built using a 2D anisotropic turbulence spectrum (see Section 4.2.3 for more details). As highlighted by Atassi and Logue [85][86], Posson *et al.* [34], Grace *et al.* [38], and Gea-Aguilera *et al.* [87], the turbulence spectrum has a substantial impact on the acoustic power prediction. As a consequence, it is of paramount importance that the two models make use of the same turbulence spectrum. For consistency with the Liepmann model used in the 3D Posson model, the 2D version of the same spectrum has been implemented in Ventres' model. Following the methodology of Ventres *et al.* [32], the integration of the 3D Liepmann spectrum Φ_{ww}^L (see Appendix B.1) must be done over the radial wave number and the strip width Δr , with $\mathbf{k}_c = (k_{xc}, k_{yc}, k_{zc})$:

$$\int_{-\infty}^{+\infty} \int_{-\infty}^{+\infty} \Phi_{ww}^L(\mathbf{k}_c) e^{ik_{zc}\Delta r} dk_{zc} d\Delta r. \quad (20)$$

Since the variables k_{zc} and Δr are independent, and $\Phi_{ww}^L(\mathbf{k}_c)$ does not depend on Δr , the

integral defined in Eq.(20) can be rewritten in the following form:

$$\int_{-\infty}^{+\infty} \Phi_{ww}^L(\mathbf{k}_c) \int_{-\infty}^{+\infty} e^{ik_z \Delta r} d\Delta r dk_{zc} = 2\pi \Phi_{ww}^L(k_{xc}, k_{yc}, 0), \quad (21)$$

considering the definition of the delta function:

$$\int_{-\infty}^{+\infty} e^{ik_{zc} \Delta r} d\Delta r = 2\pi \delta(k_{zc}). \quad (22)$$

Eventually, the Gaussian turbulence spectrum of Nallasamy and Envia [36] is replaced by the spectrum defined in Eq. (21), which consists in the 3D Liepmann spectrum for which the radial wave number k_{zc} has been set to zero. The background and wake turbulence decomposition proposed by Nallasamy and Envia is then applied using this 2D Liepmann spectrum. The comparison between the 2D and 3D models using the Liepmann isotropic turbulence spectrum is shown in Fig. 19.

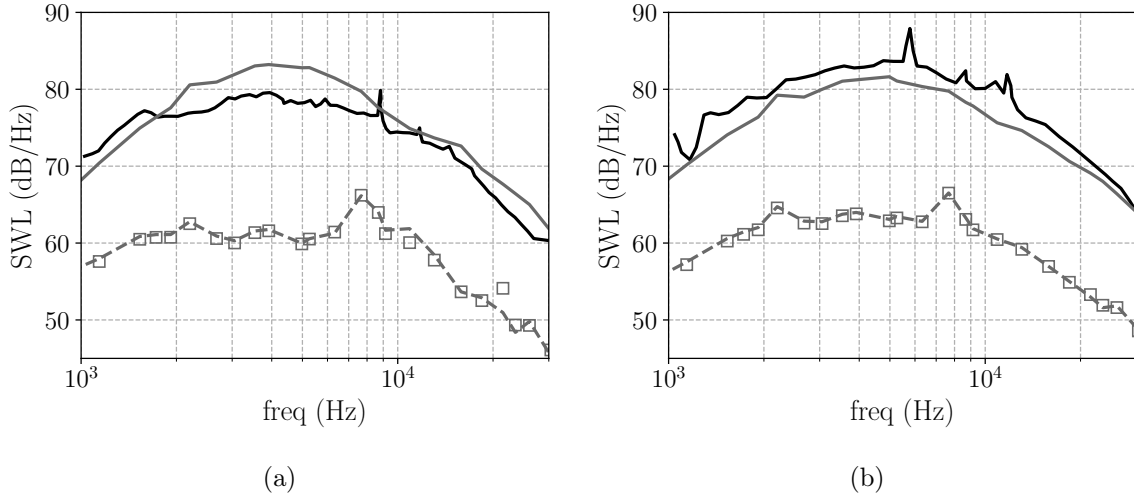


Figure 19: Comparison of the SWL of 2D and 3D models with Liepmann's spectrum (2D or 3D). Experiment (---), Posson (—), Ventres (---), Posson 2D (\square). (a) Upstream SWL, (b) Downstream SWL.

Upstream of the stator, the prediction obtained with the model of Posson tends to slightly underestimate the acoustic power below 2 kHz and overestimate it by 2 to 4 dB between 2 kHz and 8 kHz. Above 8 kHz, the prediction recovers quite faithfully the acoustic power from the experiment. However, downstream of the stator, Posson's model underestimates the acoustic power on the entire range of studied frequencies by 2 to 4 dB with respect to the experiment. Regarding the 2D models of Ventres and Posson, a significant underestimation of 10 to 18 dB can be observed for both upstream and downstream predictions. The overall shape of the predictions, however, is similar to what is observed experimentally and with the model of Posson. Similar results have been presented by Grace *et al.* [38, 39, 84], showing important discrepancies when using isotropic turbulence models, such as the Liepmann or a Gaussian spectrum, with a 2D cascade response. This analysis shows that using a 2D homogeneous and isotropic turbulence spectrum with a 2D cascade response does not lead to reliable acoustic power predictions. For 2D models, the anisotropic model of Nallasamy and Envia, as shown in Section 4.2.3, gives more satisfactory results. Nevertheless, only 3D models give results that are really consistent with experimental data, confirming that both 3D flow description and cascade response are compulsory to carry out analytically based acoustic predictions. These predictions might be improved if anisotropy could be taken into account, as wake flows are likely to carry structures

that are stretched in the local streamwise direction. However, since classical RANS models are intrinsically isotropic, taking into account anisotropic effects requires additional modeling efforts.

4.2.3. Modeling of turbulence

The description of the turbulent impinging flow can be addressed with stochastic variables to model the power spectral density. This eventually leads to [computing](#) the upwash velocity [cross-correlation](#) function, which can be expressed as a function of the turbulent spectrum (see Eq. (23)):

$$\langle \bar{w}(\mathbf{x}_1, r) \bar{w}(\mathbf{x}_2, r)^* \rangle = \iiint_{\mathbb{R}^3} \Phi_{ww}(\mathbf{k}_c, r) e^{i\mathbf{k}_c \Delta \mathbf{x}} d\mathbf{k}_c \quad (23)$$

with the superscript $*$ indicating complex conjugation, $\Delta \mathbf{x} = \mathbf{x}_2 - \mathbf{x}_1$, \mathbf{k}_c the wave number vector and Φ_{ww} the upwash turbulent spectrum. Several spectra are used to model this term. They can be divided into two categories:

- The isotropic models: these models depend only on one integral length scale and the turbulence intensity. The Liepmann and von [Kármán](#) spectra are usually the spectra of reference.
- The anisotropic models: they depend on multiple integral length scales and on the turbulence intensity. These spectra are used to model more realistically the turbulence for flows exhibiting some anisotropy. To this end, Kerschen and Gliebe [88] developed an axisymmetric turbulence spectrum to model more realistically the turbulence in turbomachinery. In the original version of the model of Ventres [32], the spectrum is approximated as a product of three Gaussian functions depending on three different coordinates and length scales. This model was specifically designed for the model of Ventres and is naturally anisotropic by construction.

The theoretical background of all these turbulence models are briefly recalled in Appendix B. As mentioned before, these models directly depend on the integral length scale that is retrieved from the RANS simulations. Yet, it has been shown by Atassi *et al.* [85], Posson *et al.* [34], Leonard *et al.* [66], and Gea-Aguilera *et al.* [87] that variations of the integral length scale estimate have a substantial impact on the predicted noise, which implies that the choice of turbulence model itself is not inconsequential and may induce significant discrepancies in the noise predictions.

4.2.3.1 Isotropic models

The turbulence near the stator LE is usually considered as isotropic since the anisotropy generated at the rotor TE tends to rapidly decay through the interstage [33]. The most popular isotropic turbulence models are Liepmann's spectrum, von [Kármán](#)'s spectrum and Gaussian isotropic models. Previous studies by Atassi *et al.* [85] have identified the impact of using these three different models with their code BB3D. Posson *et al.* [34] also studied the discrepancies in predictions using both Liepmann's and Gaussian spectra. Both authors carried out this analysis on the low-count SDT configuration. This section extends their work, examining the disparities obtained when using Liepmann's and von [Kármán](#)'s spectra for both Hanson's and Posson's models.

Figure 20 shows [the SWL difference \(\$\Delta\$ SWL\) with respect to the noise measurements obtained with Hanson's model using both isotropic turbulence models](#). Similar comments to those of Atassi *et al.* can be made about the disparities between the two predictions. For the lowest studied frequency, a maximum gap of 2.5 dB can be observed. However, for frequencies above 2 kHz,

the two SWL unexpectedly almost overlap. Indeed, the main difference between von Kármán's and Liepmann's spectra is that the associated energy models were constructed to reproduce the inertial range energy decay of $k^{-5/3}$ for the former and of k^{-2} for the latter. However, this difference in their construction only has a limited impact on the SWL.

Similar observations can be made when using Posson's model as shown in Fig. 21. In this specific case, the disparities are slightly larger: for the lowest frequencies, the gap between the predictions using the two different turbulence models can be 1 dB higher than when using Hanson's model. For medium to high frequencies, a constant gap of around 1 dB can be observed between the two turbulence models for both upstream and downstream predictions. At low frequencies, the frequency range over which the predictions with the two turbulence models do not overlap is similar for the two acoustic models.

For both acoustic models, the Liepmann spectrum recovers the overall shape of the SWL slightly better than von Kármán's, as shown by the more stable offset with the experiment observed when using Liepmann's model.

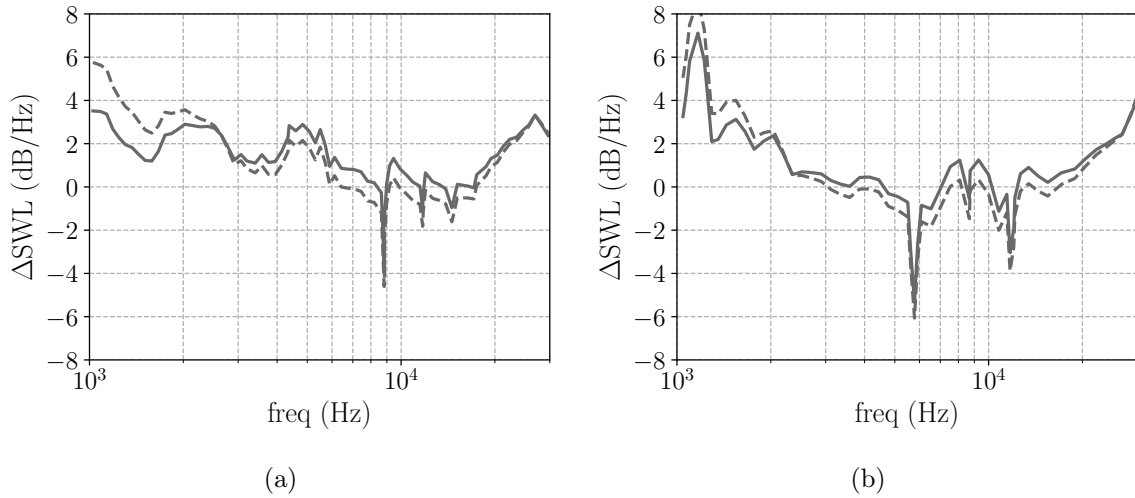


Figure 20: Predictions using Hanson's model with both Liepmann's and von Kármán's spectra. SWL difference with respect to the noise measurements. Liepmann's spectrum (—), von Kármán's spectrum (- - -). (a) Upstream Δ SWL, (b) Downstream Δ SWL.

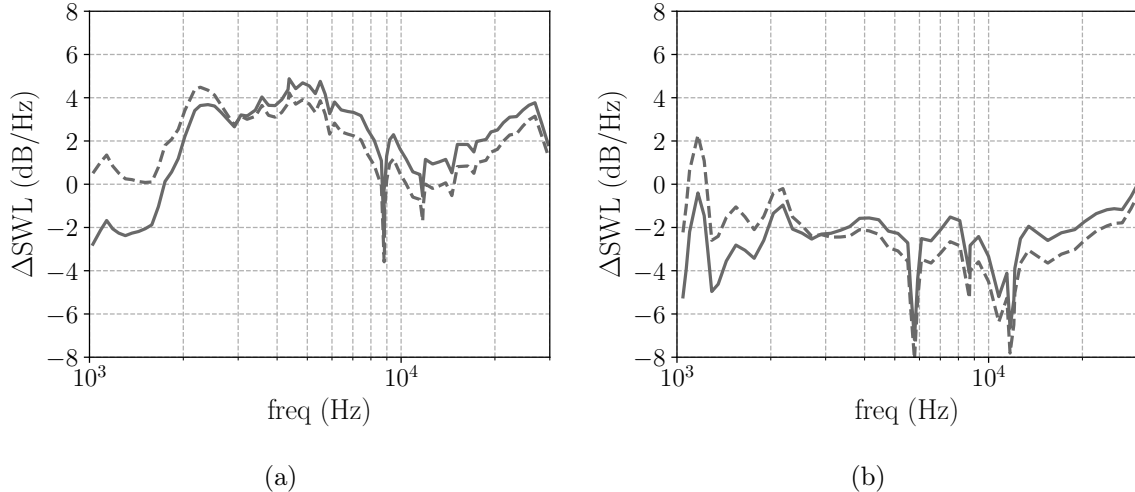


Figure 21: Predictions using Posson's model with both Liepmann's and von Kármán's spectra. [SWL difference with respect to the noise measurements](#). Liepmann's spectrum (—), von Kármán's spectrum (- - -). (a) Upstream Δ SWL, (b) Downstream Δ SWL.

4.2.3.2 Anisotropic models

As already mentioned, the flow close to the rotor TE of a fan stage can be significantly anisotropic within the wake. Nevertheless, this anisotropy significantly decreases through the interstage [33, 71], leading to a quasi-isotropic flow at the stator LE of current engine architectures. However, future engine architectures will display shortened nacelles, which will substantially decrease the spacing between the rotor and the stator, questioning the common assumption of isotropic turbulence near the stator LE. Thus, it is of great interest to assess the impact of the flow anisotropy on the predicted noise. To do so, several anisotropic models have been developed. Two of them are analyzed in the present work: the anisotropic spectrum of Nallasamy and Envia [36], which is based on previous work by Ventres, and the axisymmetric spectrum of Kerschen and Gliebe [88], based on the earlier works by Batchelor [89] and Chandrasekhar [90, 91]. The spectrum equations for both models are briefly recalled in Appendix B.2.

Figure 22 compares the predictions obtained using the model of Ventres with two different turbulence models: the 2D Liepmann spectrum presented in section 4.2.2, and Nallasamy and Envia's anisotropic spectrum [36]. At high frequency, the noise levels obtained from the model of Ventres using Nallasamy and Envia's spectrum are comparable to the SWL provided by the 3D model of Posson with Liepmann's spectrum (see Fig. 21). For low to medium frequencies, however, this model significantly under-predicts the noise, with a gap that can reach almost 7 dB with respect to the experimental data. Regarding the predictions obtained with the 2D Liepmann spectrum, the overall shape of the SWL is similar to the one obtained with Nallasamy and Envia's spectrum. Nevertheless, significant discrepancies ranging from 10 dB to 15 dB can be observed between the SWL obtained with the two turbulence models. This confirms that a 2D cascade response used in conjunction with a 2D isotropic turbulence model cannot provide reliable SWL predictions for this test case. The model of Nallasamy and Envia provides better results with the 2D cascade response. Still, the use of 3D models seems to be unavoidable to get predictions that are reasonably close to the experimental data.

Posson *et al.* [34] showed the impact of anisotropy onto the predicted noise by using the axisymmetric spectrum of Kerschen and Gliebe [88]. This preliminary study focused on the case $l_a/l_t = 2$, where l_a and l_t are the integral length scales in the direction of this axis of symmetry and in the transverse direction respectively. In order to assess the impact of anisotropy for more realistic cases, Posson's model is used in the present work with the axisymmetric spectrum

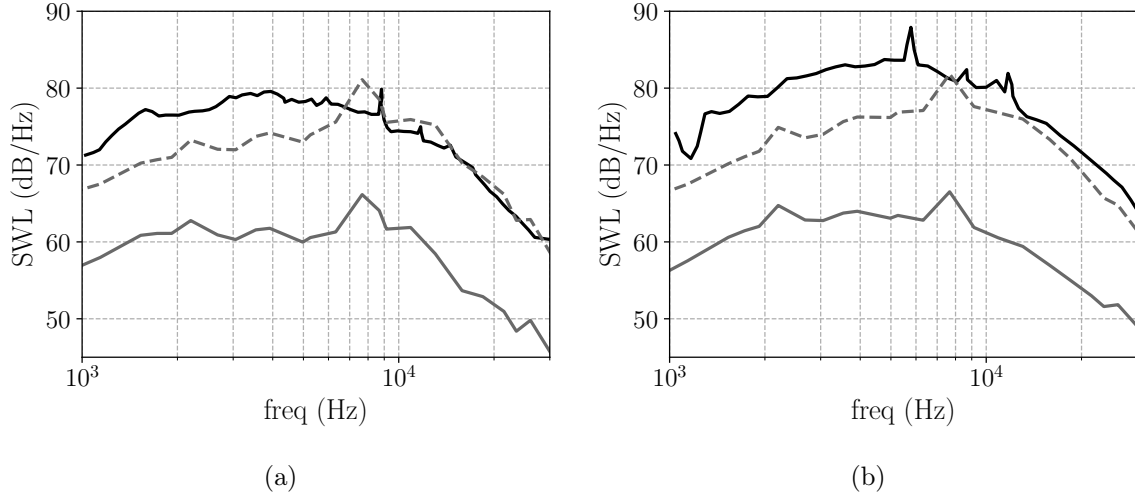


Figure 22: Predictions using [Ventres'](#) model with both [Liepmann's](#) and [Nallasamy and Envia's](#) spectra. Experiment (—), [Liepmann's](#) spectrum (---), [Nallasamy and Envia's](#) spectrum (-.-). (a) Upstream SWL, (b) Downstream SWL.

of [Kerschen and Gliebe](#) [88] for l_a/l_t ratios closer to 1, with values ranging from 0.7 to 1.5. The specific case $l_a/l_t = 1$ actually corresponds to [Liepmann's](#) spectrum. The most realistic cases are those for which $l_a/l_t > 1$, since the axial integral length scale tends to be larger than the transverse one. Predictions for $l_a/l_t < 1$ have been included for the sake of completeness. The objective of this study is more to quantify the impact of the anisotropy with respect to the isotropic case ($l_a/l_t = 1$), rather than to identify the ratio that gives results closest to the experimental data. As a consequence, only the SWL difference (Δ SWL) with respect to the isotropic case is plotted in [Figs. 23 and 24](#), which show the results obtained with [Posson's](#) model for $l_a/l_t < 1$ and $l_a/l_t > 1$, respectively. As it can be seen from [Fig. 23](#), a ratio of $l_a/l_t = 0.9$ increases the noise by 0.5 dB at low frequencies, by 1.5 dB at medium frequencies, and by 2.5 dB at high frequencies with respect to the isotropic case ($l_a/l_t = 1$). This trend is the same for each 0.1 step down to $l_a/l_t = 0.7$, reaching a maximum gap of 1.5 dB at low frequencies, of 4.5 dB at mid frequencies and of 7.5 dB at high frequencies with respect to the isotropic case. For $l_a/l_t > 1$, the trends are relatively similar: from $l_a/l_t = 1$, each increase of 0.1 in the ratio induces a decrease in the noise of 0.5 dB at low frequencies, of 1.5 dB at mid frequencies and of 2.5 dB at high frequencies. This behavior is consistent with what [Gea-Aguilera et al.](#) [87] observed in their study on the broadband noise produced by the interaction of anisotropic turbulence with an isolated flat plate, using [Kerschen and Gliebe's](#) spectrum along with [Amiet's](#) model. As highlighted by [Gea-Aguilera et al.](#) [87], the use of this axisymmetric spectrum changes the amount of energy that contributes to the RSI mechanism, resulting in significant noise levels disparities.

This study shows how sensitive these models are towards the flow anisotropy. A slight deviation from the isotropic case can lead to substantial modifications in the predicted noise, indicating that the anisotropy of the flow must be accurately measured and assessed in order to ensure reliable analytical noise predictions.

4.3. Computation of the acoustic sources: cascade effect

Previous studies by [Cheong et al.](#) [21], [Jenkins et al.](#) [92], [Blandeau et al.](#) [79] and [Gea-Aguilera et al.](#) [80] have shown that the cascade effect on the SWL becomes negligible at high frequencies. These studies were carried out using 2D approaches for both cascade and isolated-airfoil models, on a single radial position and considering a free-field propagation. [Posson](#)

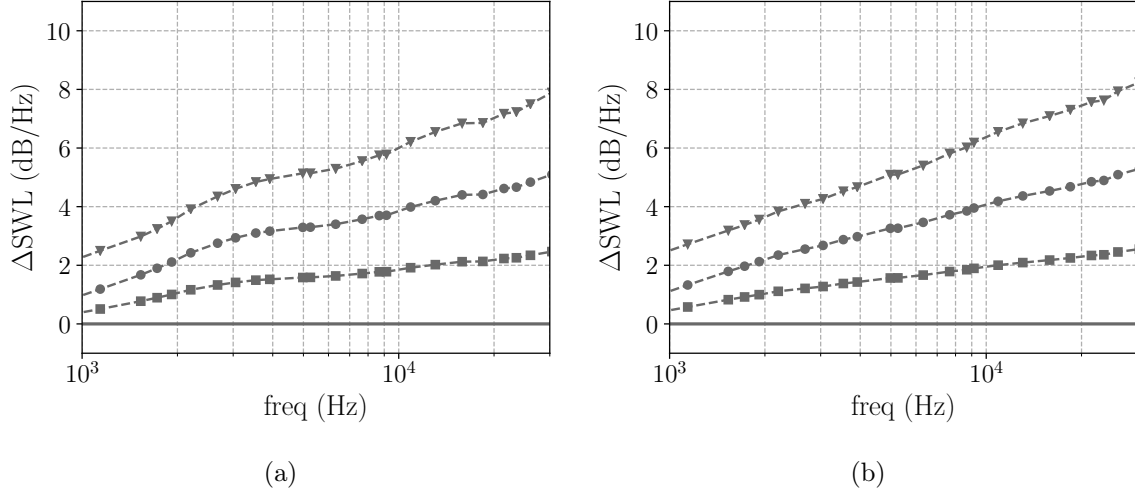


Figure 23: Predictions using Posson's model with Kerschen and Gliebe's spectrum ($l_a/l_t < 1$). SWL difference with respect to the isotropic case ($l_a = l_t$). $l_a = l_t$ (—), $l_a = 0.9l_t$ (-■-), $l_a = 0.8l_t$ (-●-), $l_a = 0.7l_t$ (-▼-). (a) Upstream Δ SWL, (b) Downstream Δ SWL.

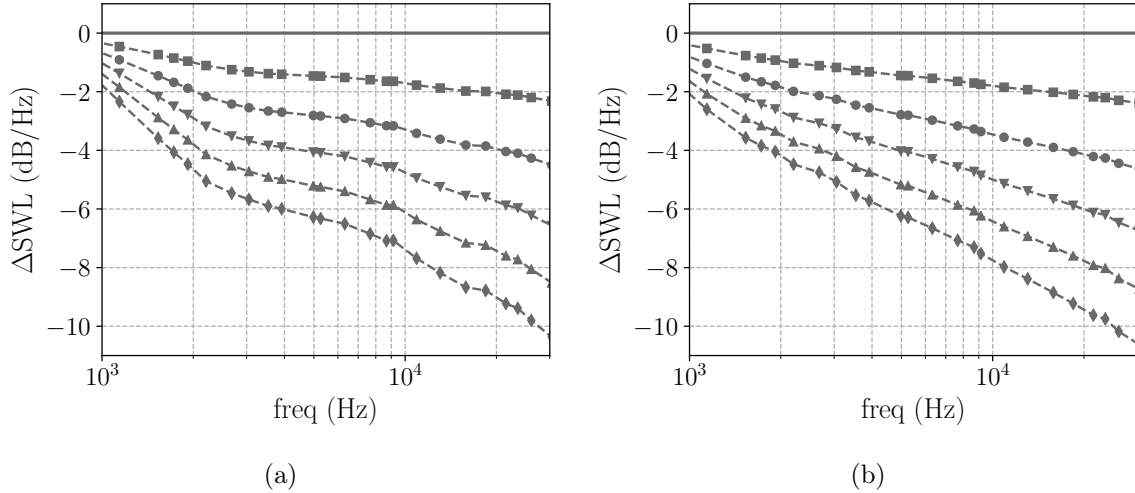


Figure 24: Predictions using Posson's model with Kerschen and Gliebe's spectrum ($l_a/l_t > 1$). SWL difference with respect to the isotropic case ($l_a = l_t$). $l_a = l_t$ (—), $l_a = 1.1l_t$ (-■-), $l_a = 1.2l_t$ (-●-), $l_a = 1.3l_t$ (-▼-), $l_a = 1.4l_t$ (-▲-), $l_a = 1.5l_t$ (-◆-). (a) Upstream Δ SWL, (b) Downstream Δ SWL.

et al. [47] also carried out a study on the cascade effect by comparing the unsteady loading obtained from the 3D Posson model with an isolated airfoil response. Posson *et al.* [47] pointed out that for a blade overlap close to zero, with small to moderate solidity, the cascade response gets closer to the response of an isolated airfoil. Some significant disparities however appear for high-solidity configurations. Grace [61] obtained similar results on the SDT configuration using a 3D approach similar to that of Posson. Grace showed that the vane responses provided by the single airfoil and the cascade methods do not agree for high-solidity configurations, even at high frequency. Grace also showed that these vane response disparities lead to a significant underestimation of the radiated noise when using a single airfoil-based approach. Both Posson *et al.*'s [47] and Grace's [61] 3D studies seem to contradict the results obtained in a 2D context.

This section further investigates this question by presenting an assessment of the impact of the cascade effect on the sound power. More precisely, the objective of this part is to determine if the single airfoil and the cascade responses lead to similar acoustic power spectra for 3D

analytical models, especially at high frequencies.

In the 3D Posson model, the computed cascade response is actually the pressure jump $\Delta\hat{P}_0$ through the vanes. As proposed by Grace [61], a direct way to neglect the cascade effect is to replace this response with a 3D isolated profile response such as the one of Amiet’s model [10, 11, 12, 13], which corresponds to the Amiet’s model implementation described in Section 2.2. Since the integration of the pressure jump of Amiet’s response is performed numerically, a convergence study has been carried out to guarantee the convergence of the presented results in terms of the number of points to discretize the chord.

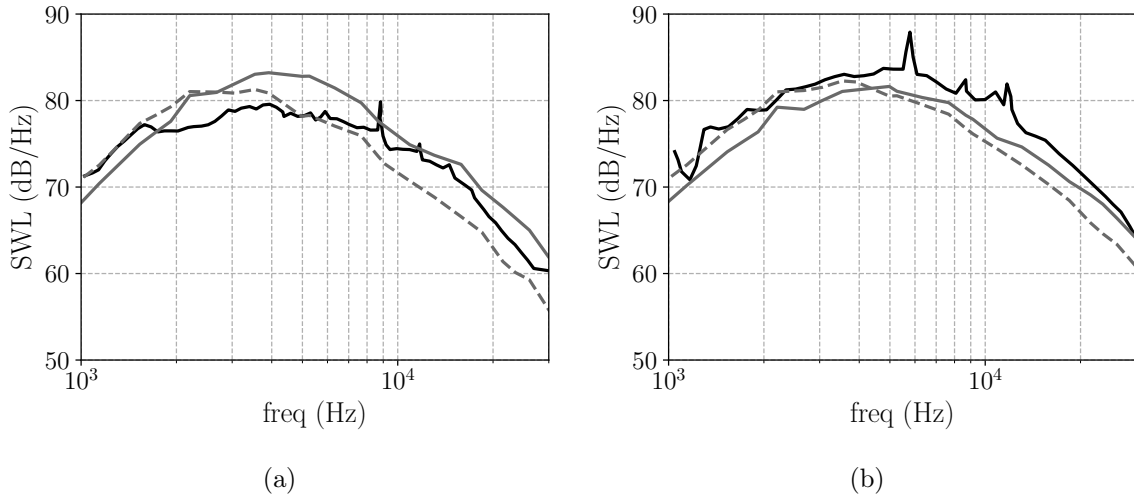


Figure 25: Cascade effect, baseline configuration. Experiment (—), Posson (—), Amiet 3D (- - -). (a) Upstream SWL, (b) Downstream SWL.

Figure 25 shows the acoustic power radiated upstream and downstream of the SDT baseline configuration stage obtained following two approaches: the 3D Posson model either including the cascade response or considering a 3D Amiet independent response for each vane of the row as explained above. Since only the vane response is modified, the noise propagation step takes the duct walls into account for both computations. The upstream prediction displays the major discrepancies between the two models. Below 2 kHz, a gap of 2 dB can be observed between the predictions. Above 2 kHz, the two predictions significantly differ by a gap ranging from 3 to 5 dB. For the downstream SWL, a gap of 2 dB can be observed over almost the entire studied frequency range.

This first study tends to confirm that, even at high frequencies, the cascade effect has a significant impact on the predicted acoustic power. The relatively high solidity of the chosen configuration may be partly responsible for such important disparities between the two models. In order to confirm this hypothesis, a second test case, based on the baseline configuration, has been defined by dividing the number of vanes by 2 while keeping the same vane geometry and input parameters. This results in a reduced configuration with 27 vanes and halved solidity and vane overlap. Figure 26 shows the SWL difference ΔSWL between the predictions using Posson’s and Amiet’s models obtained for both configurations. For both upstream and downstream predictions, the gap between the two models has been radically reduced with the 27-vane configuration with respect to the 54-vane configuration. For the upstream prediction using the 27-vane configuration, the predictions overlap for low frequencies and a maximum gap of 2 dB is observed between the two models for medium and high frequencies. The downstream predictions provided by both models are almost identical with the 27-vane configuration.

This confirms that, even at high frequencies the cascade effect cannot be neglected in realistic turbofan geometries, and that its impact on the predicted noise is even more significant for

configurations with high solidity and vane overlap. Thus, this analysis extends the conclusions drawn by Posson *et al.* [47] about the unsteady loading to the resulting acoustic power spectrum, and simultaneously confirms Grace’s results [61]. The results of this study are not consistent with what has been observed in most of the literature so far [21, 92, 79, 80]. However, the differences are most likely attributed to the fact that in the present study, 3D models with an in-duct acoustic analogy have been used whereas the other studies used 2D models with a free-field analogy.

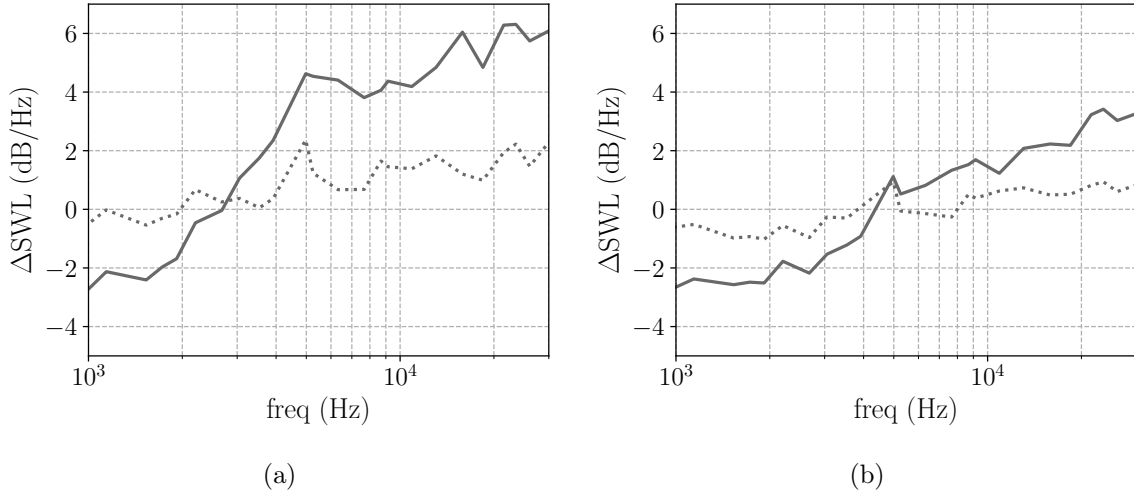


Figure 26: Cascade effect. SWL difference between Posson’s model and Amiet’s model predictions. Baseline configuration with 54 vanes (—), Reduced configuration with 27 vanes (⋯). (a) Upstream Δ SWL, (b) Downstream Δ SWL.

The cascade effect can be clearly observed when analyzing the amplitude of the duct modes produced by each model. Figure 27 shows the difference between the modal amplitudes obtained with Posson’s model and those obtained with Amiet’s in the baseline configuration. The cascade effect is significant at high frequencies and for high order modes. This is especially the case above 20 kHz in the upstream direction, for which Posson’s model predicts modal amplitudes that can be 6 to 8 dB higher than those produced by Amiet’s, particularly for the co-rotating modes. In the downstream direction, the contra-rotating modes are the most affected by the cascade effect, mainly for azimuthal orders higher than 70. The Δ SWL is much smaller in the downstream direction than in the upstream one, as observed on the SWL spectra. The peak values observed at each cut-off frequency results from the non-coincidence of the cut-off frequencies of the duct-modes with that of the linear cascade which results in unphysical resonances with Posson’s model.

Similar modal maps have been plotted for the baseline case with 27 vanes in Fig. 28. As expected, the cascade effect is much less significant for this configuration, since lower modal amplitude level differences are observed at high frequency, for both upstream and downstream predictions. In the upstream direction, the co-rotating mode amplitudes produced by each model are much closer. Downstream of the OGV, the Δ SWL does not exceed 4 dB and the significant differences previously observed for the contra-rotating modes have been significantly reduced.

4.4. Influence of the propagation type: free-field propagation or in-duct propagation with mean uniform or swirling flow

The radiation part of these models is a determinant step in the prediction of the broadband interaction noise. Three main acoustic analogies are used: the model of Hanson propagates the sound within each strip with a mean axial flow whereas the models of Posson and Ventres resort

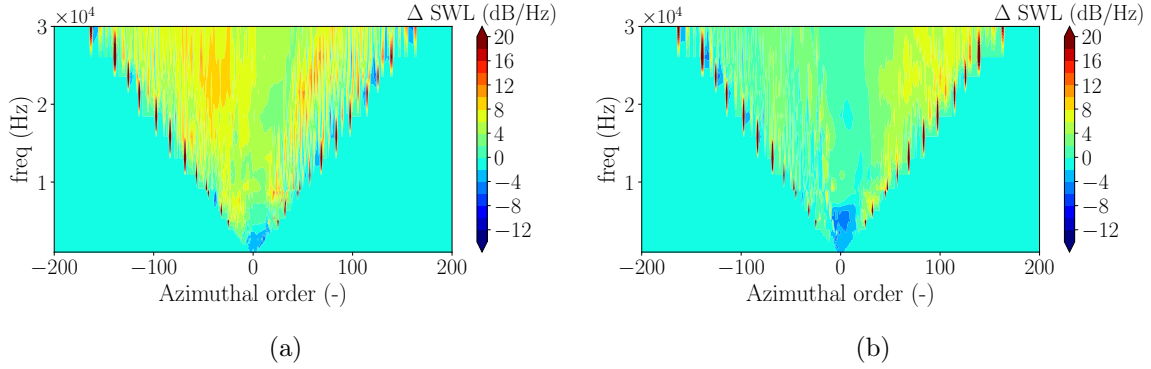


Figure 27: Modal amplitude difference between Posson's and Amiet's models. (a) Upstream Δ SWL, (b) Downstream Δ SWL.

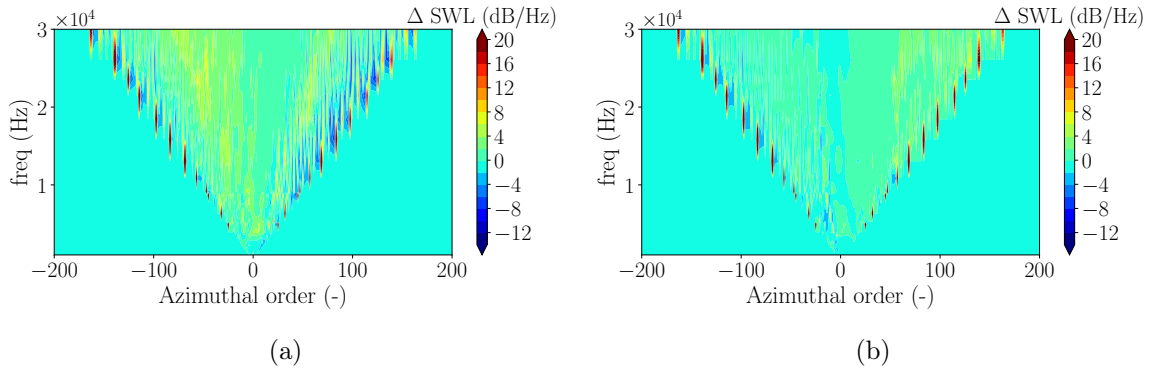


Figure 28: Modal amplitude difference between Posson's and Amiet's models, baseline configuration with 27 vanes. (a) Upstream Δ SWL, (b) Downstream Δ SWL.

to the in-duct analogy with a mean axial flow developed by Goldstein [59], and Masson's model to the in-duct analogy with a mean swirling flow developed by Posson and Peake [50].

This section addresses the impact of the chosen acoustic analogy on the broadband noise prediction. Considering only homogeneous turbulence, through the use of the Liepmann spectrum, the main differentiating parameter between the models of Hanson, Posson, and Masson is the radiation step since they all make use of Glegg's cascade response.

Figure 29 shows the upstream and downstream SWL obtained from Hanson's, Posson's and Masson's models. At low frequencies, for both the upstream and downstream predictions, the model of Hanson tends to overestimate the radiated noise contrary to the model of Posson. This is due to the fact that in the annular duct analogy, the duct cut-off effect is accounted for, leading to a reduced noise radiation especially at low frequencies. Upstream of the stator, these two models give relatively similar noise predictions at high frequencies. However, at medium frequencies, the model of Posson tends to overestimate the noise. This is partially corrected when accounting for the upstream swirling flow as shown by Masson's model prediction, which displays lower noise levels at medium frequencies than those of Posson's model, but similar ones at low and high frequencies. The downstream predictions display significant differences between Hanson's and Posson's models. For Posson's model, a constant gap of at least 3.4 dB is observed over the entire range of studied frequencies. Hanson's model, however, gives satisfactory results, especially for frequencies between 3 kHz and 20 kHz for which it faithfully recovers the experimental acoustic noise levels. Outside of this range, the model of Hanson overestimates the SWL especially at low frequencies, as with the upstream prediction. **Yet, the gap of 3 dB is most likely needed because of the reflection on the rotor blades [82, 83].** This phenomenon is significant in the case

of the SDT configuration in which the hub to tip ratio is $H = \frac{R_{\text{Hub}}}{R_{\text{Tip}}} = 0.5$. In future UHBR engine architectures, this ratio should decrease in conjunction with an increase in the bypass ratio, resulting in a reduction of the cut-off effect of the duct geometry. Regarding the overall shape of the spectra, Masson’s and Hanson’s model seem to better recover the shape of the upstream experimental spectrum, whereas Posson’s model prediction is closer to the experimental spectrum shape in the downstream direction.

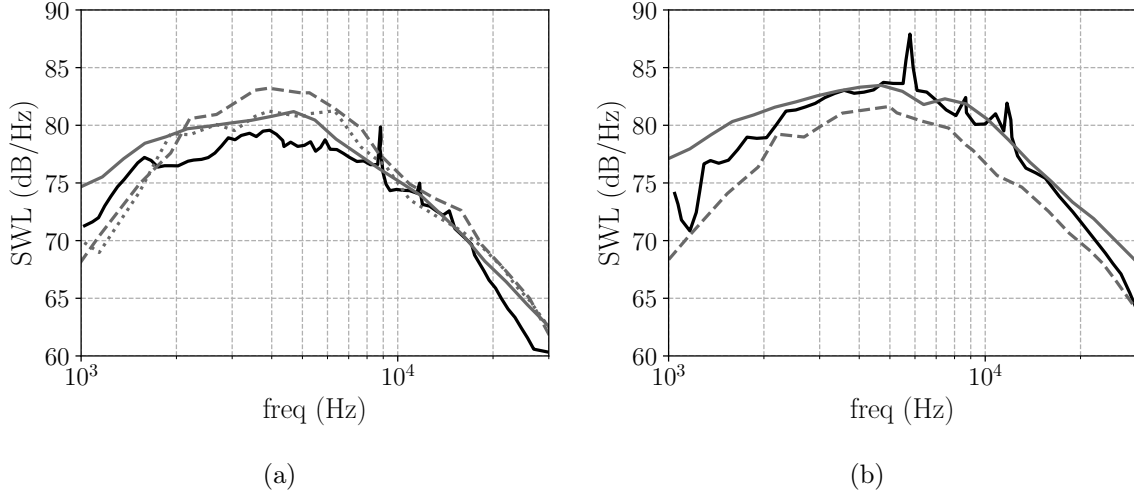


Figure 29: Propagation effect. Experiment (—), Hanson (—), Posson (- - -), Masson (····). (a) Upstream SWL, (b) Downstream SWL.

5. Conclusion

A comprehensive noise computation of the NASA SDT baseline configuration, at approach condition has been performed using RANS-informed analytical models. Four of the most advanced analytical models taking the cascade effect into account have been tested in order to identify the impact of the assumptions made in the models on the noise predictions. The models have shown to be significantly dependent on the chosen stagger angle to model the equivalent flat plate geometry for the model. Substantial disparities have been observed especially in the upstream SWL whereas the impact on the downstream predictions is limited. The modeling of the impinging flow has then been investigated, showing great dependency with the accuracy of the RANS simulation from which the input parameters are extracted. Modeling the impinging flow and the cascade response in 3D has been shown to be compulsory to correctly recover the noise levels without relying on anisotropic turbulence models. A limited difference between the noise predictions when using Liepmann’s and von Kármán’s isotropic spectra has been observed. However, using the axisymmetric turbulence model of Kerschen and Gliebe has shown that the tested models are very sensitive to anisotropy and that it must be carefully configured to ensure reliable predictions. The present work has also confirmed that, for modern fan-OGV stages, isolated airfoil responses cannot faithfully predict the radiated noise since the cascade effect is too significant for the studied range of cascade solidity values. Finally, the type of acoustic analogy used to propagate the sound has shown to be a determinant choice in building the models. It has a substantial impact on both the shape and the absolute noise levels: accounting for the duct cut-off effect reduces the low-frequency noise while the swirling flow predicts lower noise levels at medium frequencies.

6. Acknowledgments

This work was supported by several funding sources: D.L. received funding from the European Union’s Horizon 2020 research and innovation program under grant agreement No. 690714 (project TurbonoiseBB), J.d.L. received funding from NSERC (Natural Sciences and Engineering Research Council of Canada) and V.M. was funded by Airbus through the Industrial Chair in Aeroacoustics at Université de Sherbrooke.

This work was performed within the framework of the LABEX CeLyA (ANR-10-LABX- 0060) of Université de Lyon, within the program ‘Investissements d’Avenir’ (ANR-16- IDEX-0005) operated by the French National Research Agency (ANR).

The computational resources were provided by CERFACS.

The authors would like to thank E. Envia from NASA for providing the experimental data in the framework of the AIAA benchmark.

Appendix A. Convergence study of the model of Ventres

This section is dedicated to the assessment of the number of points required to guarantee that Ventres’ cascade response is converged. Figure A.1 shows the evolution of the SWL predicted by Ventres’ model for various number of discretization points, using the RANS data from Nallasamy and Envia [36]. The increase in the number of points only affects the SWL at high frequencies for which only slight modifications can be observed. The 500-point discretization is the highest level of refinement that could be reached on the cluster used for the computation.

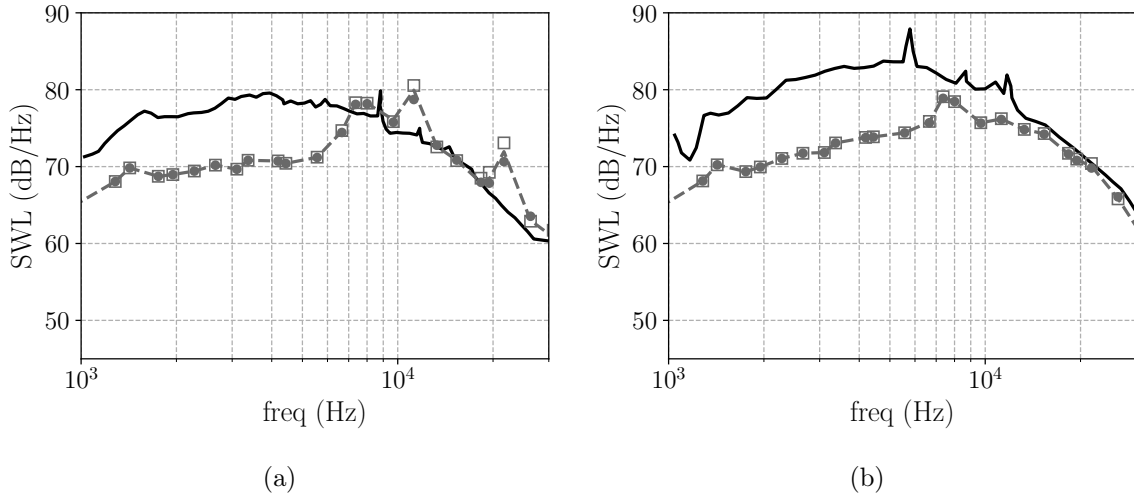


Figure A.1: Comparison of the SWL of the original Ventres model for different number of discretization points using the anisotropic spectrum of Nallasamy and Envia [36]. Experiment (—), 300 pts (●), 400 pts (---), 500 pts (□). (a) Upstream SWL, (b) Downstream SWL.

Figure A.2 shows the comparison between the most refined prediction using Ventres’ model and the 2D model of Posson presented in section 4.2.2. The results from Nallasamy and Envia [36] are also plotted on the same figure. Even though they used an approach based on Ventres’ model, the code has been significantly updated and is now called RSI (Rotor-Stator Interaction). The latest implementation of the code, however, is not available for our study. The discrepancies between their results and the Ventres implementation used in the present article illustrate the successive upgrades of the code. Indeed, in Fig. A.2, it should be noted that the downstream and upstream predictions obtained with the 2D Posson model and the original model of Ventres are almost identical, ensuring the convergence of the original Ventres response. For the upstream SWL, however, a difference for a frequency at around 11 kHz can be observed. This disparity

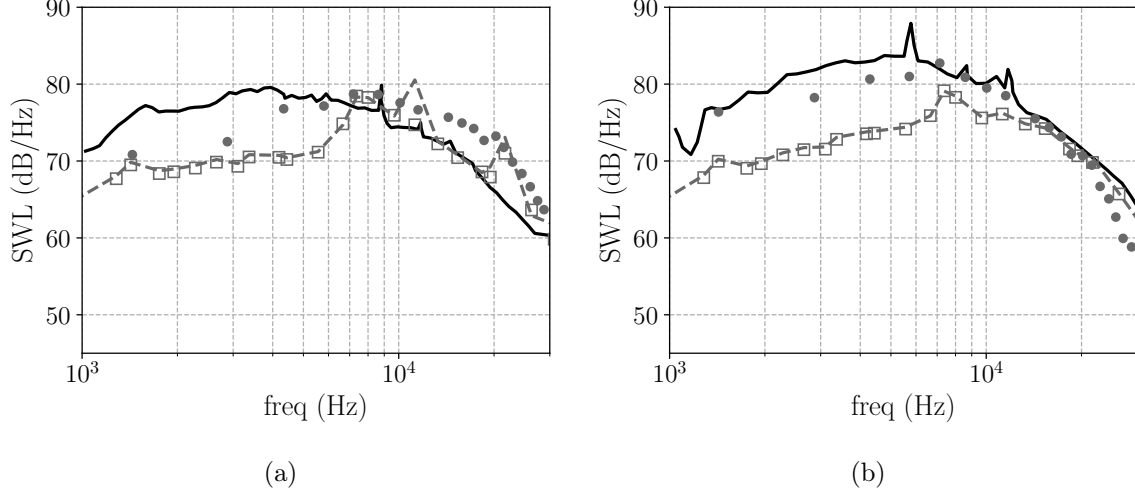


Figure A.2: Comparison of the SWL of the original Ventres model and the Ventres model with the 2D Posson response using the anisotropic spectrum of Nallasamy and Envia [36]. Experiment (—), Nallasamy and Envia's result (●), Ventres - 500 pts (---), Posson 2D (□). (a) Upstream SWL, (b) Downstream SWL.

may be due to the lack of discretization points required to compute the Ventres cascade response. However this isolated difference does not put the convergence of the cascade response into question since the predictions obtained from the two models overlap on the rest of the studied frequency range. [Ventres'](#) cascade response is then considered reliable for this configuration when using 500 points.

Appendix B. Turbulence models

As mentioned in Section 4.2.3, the use of turbulence models is compulsory to compute the upwash velocity cross-correlation function. This section presents the models used in the present work.

B.1. Isotropic turbulence models

B.1.1. Liepmann's turbulence model

Locally isotropic homogeneous turbulence can be modeled using Liepmann's spectrum. A convenient way to compute the upwash turbulence spectrum Φ_{ww} is to express it in the cascade reference frame as detailed in [34]. In this reference frame, the upwash turbulence spectrum divided by the turbulence intensity is:

$$\Phi_{ww} = \Phi_{2,2} = \Phi_{ww}^{\text{Liep}}(\mathbf{k}_c) = \frac{2\Lambda^5}{\pi^2} \frac{k_{x_c}^2 + k_{z_c}^2}{(1 + \Lambda^2 k_s^2)^3} \quad (\text{B.1})$$

where $k_s^2 = k_{x_c}^2 + k_{y_c}^2 + k_{z_c}^2$.

B.1.2. von Kármán's turbulence model

Similarly, von Kármán's spectrum for the upwash velocity in the cascade reference frame, as detailed in [78], is:

$$\Phi_{ww}^{VK}(\mathbf{k}_c) = \frac{55\Gamma(5/6)}{36\pi^{3/2}\Gamma(1/3)k_e^3} \frac{k_{x_c}^2 + k_{z_c}^2}{\left[1 + \left(\frac{k_s}{k_e}\right)^2\right]^{17/6}} \quad (\text{B.2})$$

where $k_e = \frac{\sqrt{\pi}\Gamma(5/6)}{\Lambda\Gamma(1/3)}$ and $\Gamma()$ is the Gamma function.

B.2. Anisotropic turbulence models

B.2.1. Axisymmetric turbulence model

The axisymmetric model used in the present work has been developed by Kerschen and Giebe [88]. The following equation defines the three-dimensional cross-spectrum of the i and j components of the turbulence velocity in Cartesian coordinates:

$$\Phi_{ij}(\mathbf{k}) = [k^2 \delta_{i,j} - k_i k_j] F + [(k^2 - (\mathbf{k} \cdot \boldsymbol{\lambda})^2) \delta_{i,j} - k_i k_j - k^2 \lambda_i \lambda_j + \mathbf{k} \cdot \boldsymbol{\lambda} (\lambda_i k_j + \lambda_j k_i)] G \quad (\text{B.3})$$

where

$$F = \frac{F_0}{(1 + l_a^2 k_a^2 + l_t^2 k_t^2)^3}, \quad F_0 = \frac{2u_a^2 l_a l_t^4}{\pi^2}, \quad G = BF \quad \text{and} \quad B = \frac{2u_t^2}{u_a^2} - \frac{l_t^2}{l_a^2} - 1. \quad (\text{B.4})$$

$\boldsymbol{\lambda}$ is a unit vector in the direction of the symmetry axis. k_a is the wavenumber in the direction of the symmetry whereas k_{ty} and k_{tz} are the wavenumbers in the transverse directions which define the magnitude of the transverse wavenumber $k_t = \sqrt{k_{ty}^2 + k_{tz}^2}$. u_a and u_t correspond to the root mean square values of the velocity fluctuations along the axis of symmetry and in the transverse direction respectively. The integral [length scales](#) l_a and l_t are correspondingly defined along the axis of symmetry and in the transverse direction. These variables must comply with the following constraint:

$$2 \frac{u_t^2}{u_a^2} \geq \frac{l_t^2}{l_a^2}.$$

Eq. (B.3) corresponds to the spectrum in Cartesian coordinates and cannot be directly used to compute the upwash velocity cross-correlation. To do so, a change of reference frame from the duct reference frame to the cascade reference frame needs to be performed. This is out of the scope of this article but a detailed calculation of the equation of the upwash cross-correlation (recalled in Eq. (B.5)) has been performed by Posson *et al.* [34].

$$\Phi_{ww}(\mathbf{k}_c) = \left[k_{x_c}^2 + k_{z_c}^2 + B \left(\tilde{\mathbf{Q}}_{31} k_{x_c} - \tilde{\mathbf{Q}}_{11} k_{z_c} \right)^2 \right] F, \quad (\text{B.5})$$

where $\tilde{\mathbf{Q}}$ is the transformation matrix from the duct reference frame to the cascade reference frame.

B.2.2. Ventres' turbulence model

In the original implementation of Ventres' model, the turbulence spectrum only takes the background turbulence into account. It has then been enhanced by Nallasamy and Envia by splitting the impinging flow into a background and a wake contribution.

In this section, the original spectrum of Ventres is briefly presented to emphasize its inherent anisotropic construction. The original spectrum defines the velocity cross-correlation as a product of three Gaussian correlation functions, each of them depending only on one coordinate in the duct reference frame:

$$\Phi(x_c, y_c, \Delta r) = \Phi_{x_c}(x_c/\Lambda_{x_c}) \Phi_{y_c}(y_c/\Lambda_{y_c}) \Phi_r(\Delta r/\Lambda_r), \quad (\text{B.6})$$

where Λ_i is the integral length scale in each direction. As pointed out by Grace *et al.* [38], Eq. (B.6) defines an anisotropic turbulence because of its multiplying form. The correlation functions Φ being Gaussian functions, the turbulence [power](#) spectral density which corresponds to the double Fourier transform of Eq. (B.6) in the (x_c, y_c) plane, is defined as:

$$\hat{\Phi}_{ww}(\mathbf{k}_c, \Delta r) = \Lambda_{xc} \Lambda_{yc} \hat{\Phi}_{xc}(k_{xc} \Lambda_{xc}) \hat{\Phi}_{yc}(k_{yc} \Lambda_{yc}) \Phi_r(\Delta r / \Lambda_r), \quad (\text{B.7})$$

where $\mathbf{k}_c = (k_{xc}, k_{yc}, 0)$ is the wave number in the (x_c, y_c) plane, $\hat{\Phi}_{ww}$ is the double Fourier transform of Φ_{ww} in the (x_c, y_c) plane, $\hat{\Phi}_{xc}$ is the Fourier transform of Φ_{xc} along x_c and $\hat{\Phi}_{yc}$ is the Fourier transform of Φ_{yc} along y_c . This model also assumes that the radial integral length scale is small, leading to:

$$\int_{-L_r}^{+L_r} \Phi_r(\Delta r / \Lambda_r) d\Delta r \approx \int_{-\infty}^{+\infty} \Phi_r(\Delta r / \Lambda_r) d\Delta r = \Lambda_r \quad (\text{B.8})$$

where $L_r = l_r/2$ and l_r is the radial correlation length.

The spectrum defined by Eqs. (B.7) and (B.8) does not depend on the radial wave number, which confirms it is a 2D model. The enhancements added by Nallasamy and Envia, which are included in the implementation used in the present work, are detailed in [36].

References

- [1] S. Gu erin, C. Kissner, P. Seeler, R. A. Blazquez Navarro, P. Carrasco Lara na, H. de Laborderie, D. Lewis, C. Paruchuri, C. Polacsek, ACAT1 Benchmark of RANS-informed Analytical Methods for Fan Broadband Noise Prediction: Part II - Influence of the Acoustic Models, in: *Acoustics, Multidisciplinary Digital Publishing Institute*, 2020.
- [2] S. Moreau, in: *Fundamentals of High Lift for Future Civil Aircraft*, Springer Nature Switzerland AG, 2021, Ch. 10: A Review of Turbomachinery Noise: From Analytical Models to High-Fidelity Simulations.
- [3] D. Hanson, K. Horan, Turbulence/cascade interaction-spectra of inflow, cascade response, and noise, in: *4th AIAA/CEAS Aeroacoustics Conference*, no. 1998-2319, Toulouse, France, 1998.
- [4] C. Kissner, S. Gu erin, P. Seeler, M. Billson, C. Paruchuri, P. Carrasco Lara na, H. de Laborderie, B. Fran ois, K. Lefarh, D. Lewis, G. Montero Villar, T. Nod -Langlois, ACAT1 Benchmark of RANS-informed Analytical Methods for Fan Broadband Noise Prediction: Part I - Influence of the RANS Simulation, in: *Acoustics, Multidisciplinary Digital Publishing Institute*, 2020.
- [5] S. Moreau, M. Roger, Advanced noise modeling for future propulsion systems, *International Journal of Aeroacoustics* 17 (6-8) (2018) 576–599.
- [6] S. Moreau, Turbomachinery noise predictions: present and future, in: *Acoustics*, Vol. 1, Multidisciplinary Digital Publishing Institute, 2019, pp. 92–116.
- [7] K. B. Kontos, R. E. Kraft, P. R. Gliebe, Improved NASA-ANOPP Noise Prediction Computer Code for Advanced Subsonic Propulsion Systems, Tech. Rep. NASA-CR-195480, NASA (1996).
- [8] L. Lopes, C. Burley, Design of the next generation aircraft noise prediction program: ANOPP2, in: *17th AIAA/CEAS Aeroacoustics Conference (32nd AIAA Aeroacoustics Conference)*, no. 2011-2854, Portland, Oregon, 2011.
- [9] W. R. Sears, Some aspects of non-stationary airfoil theory and its practical application, *Journal of the Aeronautical Sciences* 8 (3) (1941) 104–108.
- [10] R. K. Amiet, Acoustic radiation from an airfoil in a turbulent stream, *Journal of Sound and Vibration* 41 (4) (1975) 407–420.
- [11] R. Paterson, R. Amiet, Acoustic radiation and surface pressure characteristics of an airfoil due to incident turbulence, in: *3rd AIAA Conference*, no. 1976-571, Palo Alto, CA, U.S.A., 1976.
- [12] S. Moreau, M. Roger, V. Jurdic, Effect of angle of attack and airfoil shape on turbulence-interaction noise, in: *11th AIAA/CEAS aeroacoustics conference*, no. 2005-2973, Monterey, California, 2005.
- [13] M. Roger, S. Moreau, A. Guedel, Broadband fan noise prediction using single-airfoil theory, *Noise Control Engineering Journal* 54 (1) (2006).
- [14] M. R. Myers, E. J. Kerschen, Influence of camber on sound generation by airfoils interacting with high-frequency gusts, *Journal of Fluid Mechanics* 353 (1997) 221–259.
- [15] M. R. Myers, E. J. Kerschen, Influence of incidence angle on sound generation by airfoils interacting with high-frequency gusts, *Journal of Fluid Mechanics* 292 (1995) 271–304.
- [16] I. Evers, N. Peake, Noise generation by high-frequency gusts interacting with an airfoil in transonic flow, *Journal of Fluid Mechanics* 411 (2000) 91–130.
- [17] S. Kaji, T. Okazaki, Generation of sound by rotor-stator interaction, *Journal of Sound and Vibration* 13 (3) (1970) 281–307.
- [18] D. S. Whitehead, *AGARD Manual on Aeroelasticity in Axial-Flow Turbomachines*. Volume 1. Unsteady Turbomachinery Aerodynamics, Chapter 3, 1987.

- [19] D. S. Whitehead, Vibration and sound generation in a cascade of flat plates in subsonic flow, Tech. Rep. 3685, Procurement executive ministry of defence aeronautical research council reports and memoranda, University of Cambridge (1970).
- [20] S. N. Smith, Discrete frequency sound generation in axial flow turbomachines, Tech. Rep. 3709, Procurement executive ministry of defence aeronautical research council reports and memoranda, University of Cambridge (1971).
- [21] C. Cheong, P. Joseph, S. Lee, High frequency formulation for the acoustic power spectrum due to cascade-turbulence interaction, *The Journal of the Acoustical Society of America* 119 (1) (2006) 108–122.
- [22] V. Jurdic, A. Moreau, P. Joseph, L. Enghardt, J. Coupland, A comparison between measured and predicted fan broadband noise due to rotor-stator interaction, in: 13th AIAA/CEAS Aeroacoustics Conference (28th AIAA Aeroacoustics Conference), no. 2007-3692, Rome, Italy, 2007.
- [23] A. Lloyd, N. Peake, Rotor-stator broadband noise prediction, in: 14th AIAA/CEAS Aeroacoustics Conference (29th AIAA Aeroacoustics Conference), no. 2008-2840, Vancouver, British Columbia, Canada, 2008.
- [24] M. E. Goldstein, in: *Aeroacoustics*, New York, McGraw-Hill International Book Co., 1976. 305 p., 1976, Ch. 5 : Theories Based on Solution of Linearized Vorticity - Acoustic Field Equations.
- [25] M. E. Goldstein, in: *Aeroacoustics*, New York, McGraw-Hill International Book Co., 1976. 305 p., 1976, Ch. 4 : Effect of Uniform Flow.
- [26] H. Atassi, G. Hamad, Sound generated in a cascade by three-dimensional disturbances convected in a subsonic flow, in: 7th Aeroacoustics Conference, no. 1981-2046, Palo Alto, CA, U.S.A., 1981.
- [27] M. Namba, Three-dimensional analysis of blade force and sound generation for an annular cascade in distorted flows, *Journal of Sound and Vibration* 50 (4) (1977) 479–508.
- [28] M. Namba, AGARD Manual on Aeroelasticity in Axial-Flow Turbomachines. Volume 1. Unsteady Turbomachinery Aerodynamics, Chapter 4, 1987.
- [29] H. Kodama, M. Namba, Unsteady Lifting Surface Theory for a Rotating Cascade of Swept Blades, *Journal of Turbomachinery* 112 (3) (1990) 411–417.
- [30] J. B. H. M. Schulten, Sound generated by rotor wakes interacting with a leaned vane stator, *AIAA Journal* 20 (10) (1982) 1352–1358.
- [31] J. B. H. M. Schulten, Vane sweep effects on rotor/stator interaction noise, *AIAA Journal* 35 (6) (1997) 945–951.
- [32] C. Ventres, M. Theobald, W. Mark, Turbofan noise generation. volume 1: Analysis, Tech. Rep. CR-167952, NASA (1982).
- [33] C. Pérez Arroyo, T. Leonard, M. Sanjosé, S. Moreau, F. Duchaine, Large eddy simulation of a scale-model turbofan for fan noise source diagnostic, *Journal of Sound and Vibration* 445 (2019) 64–76.
- [34] H. Posson, S. Moreau, M. Roger, Broadband noise prediction of fan outlet guide vane using a cascade response function, *Journal of Sound and Vibration* 330 (25) (2011) 6153–6183.
- [35] H. D. Meyer, E. Envia, Aeroacoustic analysis of turbofan noise generation, Tech. Rep. NASA-CR-4715, NASA (1996).
- [36] M. Nallasamy, E. Envia, Computation of rotor wake turbulence noise, *Journal of Sound and Vibration* 282 (3-5) (2005) 649–678.
- [37] J. Maunus, S. Grace, D. Sondak, Effect of cfd wake prediction in a hybrid simulation of fan broadband interaction noise, in: 17th AIAA/CEAS Aeroacoustics Conference (32nd AIAA Aeroacoustics Conference), no. 2011-2875, Portland, Oregon, 2011.
- [38] S. Grace, A. Wixom, J. Winkler, D. Sondak, M. Logue, Fan broadband interaction noise modeling, in: 18th AIAA/CEAS Aeroacoustics Conference (33rd AIAA Aeroacoustics Conference), no. 2012-2269, Colorado Springs, CO, 2012.
- [39] S. M. Grace, G. Forsyth, Prediction of broadband fan exit guide vane response, in: 19th AIAA/CEAS Aeroacoustics Conference, no. 2013-2153, Berlin, Germany, 2013.
- [40] S. M. Grace, M. M. Logue, Comparison of two low-order models for the prediction of fan broadband noise, *Journal of Sound and Vibration* 431 (2018) 304–327.
- [41] R. Mani, G. Horvay, Sound transmission through blade rows, *Journal of Sound and Vibration* 12 (1) (1970) 59–83.
- [42] W. Koch, On the transmission of sound waves through a blade row, *Journal of Sound and Vibration* 18 (1) (1971) 111–128.
- [43] N. Peake, The interaction between a high-frequency gust and a blade row, *Journal of Fluid Mechanics* 241 (1992) 261–289.
- [44] N. Peake, The scattering of vorticity waves by an infinite cascade of flat plates in subsonic flow, *Wave motion* 18 (3) (1993) 255–271.
- [45] S. A. Glegg, The response of a swept blade row to a three-dimensional gust, *Journal of Sound and Vibration* 227 (1) (1999) 29–64.
- [46] D. B. Hanson, Theory for broadband noise of rotor and stator cascades with inhomogeneous inflow turbulence including effects of lean and sweep, Tech. Rep. CR-2001-210762, NASA (2001).
- [47] H. Posson, M. Roger, S. Moreau, On a uniformly valid analytical rectilinear cascade response function,

- Journal of Fluid Mechanics 663 (2010) 22–52.
- [48] H. Posson, S. Moreau, M. Roger, On the use of a uniformly valid analytical cascade response function for fan broadband noise predictions, *Journal of Sound and Vibration* 329 (18) (2010) 3721–3743.
 - [49] V. Masson, H. Posson, M. Sanjose, T. Léonard, S. Moreau, M. Roger, Fan-OGV interaction broadband noise prediction in a rigid annular duct with swirling and sheared mean flow, in: 22nd AIAA/CEAS Aeroacoustics Conference, no. 2016-2944, Lyon, France, 2016.
 - [50] H. Posson, N. Peake, The acoustic analogy in an annular duct with swirling mean flow, *Journal of Fluid Mechanics* 726 (2013) 439–475.
 - [51] J. Mathews, N. Peake, The acoustic Green’s function for swirling flow in a lined duct, *Journal of Sound and Vibration* 395 (2017) 294–316.
 - [52] P. J. Baddoo, L. J. Ayton, An analytic solution for gust-cascade interaction noise including effects of realistic aerofoil geometry: Inter-blade region, in: 2018 AIAA/CEAS Aeroacoustics Conference, no. 2018-2957, Atlanta, Georgia, 2018.
 - [53] P. J. Baddoo, L. J. Ayton, An analytic solution for gust–cascade interaction noise including effects of realistic aerofoil geometry, *Journal of Fluid Mechanics* 886 (2020).
 - [54] S. Bouley, B. François, M. Roger, S. Moreau, On a mode-matching technique for sound generation and transmission in a linear cascade of outlet guide vanes, in: 21st AIAA/CEAS Aeroacoustics Conference, no. 2015-2825, Dallas, TX, 2015.
 - [55] B. François, S. Bouley, M. Roger, S. Moreau, Analytical models based on a mode-matching technique for turbulence impingement noise on axial-flow outlet guide vanes, in: 22nd AIAA/CEAS Aeroacoustics Conference, no. 2016-2947, Lyon, France, 2016.
 - [56] L. Girier, M. Roger, H. Bériot, A. Lafitte, H. Posson, A two-dimensional model of sound transmission through curved and staggered OGV: Effect of inter-vane channel mode transitions, in: 25th AIAA/CEAS Aeroacoustics Conference, no. 2019-2690, Delft, The Netherlands, 2019.
 - [57] D. Hanson, Influence of lean and sweep on noise of cascades with turbulent inflow, in: 5th AIAA/CEAS Aeroacoustics Conference and Exhibit, no. 1999-1863, Bellevue, WA, U.S.A., 1999.
 - [58] J. E. Ffowcs Williams, D. L. Hawkings, Sound generation by turbulence and surfaces in arbitrary motion, *Philosophical Transactions of the Royal Society of London. Series A, Mathematical and Physical Sciences* 264 (1151) (1969) 321–342.
 - [59] M. E. Goldstein, *Aeroacoustics*, New York, McGraw-Hill International Book Co., 1976. 305 p., 1976.
 - [60] J. de Laborderie, V. Blandeau, T. Node-Langlois, S. Moreau, Extension of a fan tonal noise cascade model for camber effects, *AIAA Journal* 53 (4) (2014) 863–876.
 - [61] S. M. Grace, Influence of model parameters and the vane response method on a low-order prediction of fan broadband noise, *International Journal of Aeroacoustics* 15 (1-2) (2016) 131–143.
 - [62] B. de Gouville, Calcul du bruit à large bande d’un rotor caréné dû à la turbulence incidente. [Computation of the broadband noise generated by the impingement of turbulence on a ducted rotor.], Ph.D. thesis, École Centrale de Lyon (1998).
 - [63] P. Joseph, A. Parry, Rotor/wall boundary-layer interaction broadband noise in turbofan engines, in: 7th AIAA/CEAS Aeroacoustics Conference and Exhibit, no. 2001-2244, Maastricht, Netherlands, 2001.
 - [64] C. M. Bender, S. A. Orszag, *Advanced mathematical methods for scientists and engineers I: Asymptotic methods and perturbation theory*, Springer Science & Business Media, 2013.
 - [65] S. J. Majumdar, N. Peake, Three-dimensional effects in cascade-gust interaction, *Wave motion* 23 (4) (1996) 321–337.
 - [66] T. Leonard, M. Sanjose, S. Moreau, F. Duchaine, Large Eddy Simulation of a scale-model turbofan for fan noise source diagnostic, in: 22nd AIAA/CEAS Aeroacoustics Conference, no. 2016-3000, Lyon, France, 2016.
 - [67] C. Heaton, N. Peake, Algebraic and exponential instability of inviscid swirling flow, *Journal of Fluid Mechanics* 565 (2006) 279.
 - [68] E. Envia, Fan noise source diagnostics test-vane unsteady pressure results, in: 8th AIAA/CEAS Aeroacoustics Conference & Exhibit, no. 2002-2430, Breckenridge, Colorado, 2002.
 - [69] C. Hughes, Aerodynamic performance of scale-model turbofan outlet guide vanes designed for low noise, in: 40th AIAA Aerospace Sciences Meeting & Exhibit, no. 2002-0374, Reno, NV, U.S.A., 2002.
 - [70] C. Hughes, R. Jeracki, R. Woodward, C. Miller, Fan noise source diagnostic test-rotor alone aerodynamic performance results, in: 8th AIAA/CEAS Aeroacoustics Conference & Exhibit, no. 2002-2426, Breckenridge, Colorado, 2002.
 - [71] G. Podboy, M. Krupar, S. Helland, C. Hughes, Steady and unsteady flow field measurements within a NASA 22 inch fan model, in: 40th AIAA Aerospace Sciences Meeting & Exhibit, no. 2002-1033, Reno, NV, U.S.A., 2002.
 - [72] G. Podboy, M. Krupar, C. Hughes, R. Woodward, Fan noise source diagnostic test-LDV measured flow field results, in: 8th AIAA/CEAS Aeroacoustics Conference & Exhibit, no. 2002-2431, Breckenridge, Colorado, 2002.
 - [73] R. Woodward, C. Hughes, R. Jeracki, C. Miller, Fan noise source diagnostic test–far-field acoustic results, in: 8th AIAA/CEAS Aeroacoustics Conference & Exhibit, no. 2002-2427, Breckenridge, Colorado, 2002.

- [74] T.-H. Shih, W. W. Liou, A. Shabbir, Z. Yang, J. Zhu, A new $k-\epsilon$ eddy viscosity model for high Reynolds number turbulent flows, *Computers & Fluids* 24 (3) (1995) 227–238.
- [75] D. Lewis, S. Moreau, M. C. Jacob, On the use of RANS-informed analytical models to perform broadband rotor-stator interaction noise predictions, in: 25th AIAA/CEAS Aeroacoustics Conference, no. 2019-2667, Delft, The Netherlands, 2019.
- [76] T. von Kármán, Airfoil theory for non-uniform motion, *Journal of the Aeronautical Sciences* 5 (10) (1938) 379–390.
- [77] J. Premo, P. Joppa, Fan noise source diagnostic test-wall measured circumferential array mode results, in: 8th AIAA/CEAS Aeroacoustics Conference & Exhibit, no. 2002-2429, Breckenridge, Colorado, 2002. URL <https://doi.org/10.2514/6.2002-2429>
- [78] H. Posson, Fonctions de réponse de grille d’aubes et effet d’écran pour le bruit à large bande des soufflantes. [Cascade responses and shielding effect for fan broadband noise.], Ph.D. thesis, École Centrale de Lyon (2008).
- [79] V. P. Blandeau, P. F. Joseph, G. Jenkins, C. J. Powles, Comparison of sound power radiation from isolated airfoils and cascades in a turbulent flow, *The Journal of the Acoustical Society of America* 129 (6) (2011) 3521–3530.
- [80] F. Gea-Aguilera, J. Gill, X. Zhang, On the effects of fan wake modelling and vane design on cascade noise, *Journal of Sound and Vibration* 459 (2019) 114859.
- [81] P. M. Morse, K. U. Ingard, in: *Theoretical acoustics*, Princeton university press, 1986, Ch. 8.
- [82] R. Blázquez-Navarro, R. Corral, Prediction of fan acoustic blockage on fan/outlet guide vane broadband interaction noise using efficient frequency domain linearised navier-stokes solvers, *Journal of Sound and Vibration* (2021) 116033.
- [83] W. Ying, R. Fattah, S. Zhong, X. Zhang, F. Gea-Aguilera, A numerical investigation of the rotor blockage effect on cascade noise using a sliding mesh method, *Journal of Sound and Vibration* 502 (2021) 116030.
- [84] S. M. Grace, Fan broadband interaction noise modeling using a low-order method, *Journal of Sound and Vibration* 346 (1) (2015) 402–423.
- [85] H. Atassi, M. Logue, Effect of turbulence structure on broadband fan noise, in: 14th AIAA/CEAS Aeroacoustics Conference (29th AIAA Aeroacoustics Conference), no. 2008-2842, Vancouver, British Columbia, Canada, 2008.
- [86] H. Atassi, M. Logue, Fan broadband noise in anisotropic turbulence, in: 15th AIAA/CEAS Aeroacoustics Conference (30th AIAA Aeroacoustics Conference), no. 2009-3148, Miami, Florida, 2009.
- [87] F. Gea Aguilera, J. R. Gill, X. Zhang, X. Chen, T. Nodé-Langlois, Leading edge noise predictions using anisotropic synthetic turbulence, in: 22nd AIAA/CEAS Aeroacoustics Conference, no. 2016-2840, 2016.
- [88] E. J. Kerschen, P. Glibe, Noise caused by the interaction of a rotor with anisotropic turbulence, *AIAA Journal* 19 (6) (1981) 717–723.
- [89] G. Batchelor, The theory of axisymmetric turbulence, *Proceedings of the Royal Society of London. Series A. Mathematical and Physical Sciences* 186 (1007) (1946) 480–502.
- [90] S. Chandrasekhar, The theory of axisymmetric turbulence, *Philosophical Transactions of the Royal Society of London. Series A, Mathematical and Physical Sciences* 242 (855) (1950) 557–577.
- [91] S. Chandrasekhar, The decay of axisymmetric turbulence, *Proceedings of the Royal Society of London. Series A. Mathematical and Physical Sciences* 203 (1074) (1950) 358–364.
- [92] G. Jenkins, C. Powles, V. Blandeau, P. Joseph, Low and high frequency models for the prediction of noise due to cascade-turbulence interaction, in: 17th AIAA/CEAS Aeroacoustics Conference (32nd AIAA Aeroacoustics Conference), no. 2011-2826, Portland, Oregon, 2011.